The influence of interfacial joints on the structural behavior of segmental tunnel rings subjected to ground pressure

Jiao-Long Zhang[a,b], Thomas Schlappal[a], Yong Yuan[b], Herbert A. Mang[a,b], Bernhard Pichler[a,*]

[a] Institute for Mechanics of Materials and Structures, TU Wien – Vienna University of Technology, Karlsplatz 13/202, 1040 Vienna, Austria
[b] College of Civil Engineering, Tongji University, Siping Road 1239, 200092 Shanghai, China

ABSTRACT

The *local* behavior of segment-to-segment interfaces has a significant influence on the *overall* structural behavior of segmental tunnel rings subjected to ground pressure. This is quantified by means of structural simulations, combining analytical solutions of the *linear* theory of slender circular arches with *time-dependent* and *nonlinear* interface models for unreinforced and bolted interfaces. The time-dependent behavior results from creep of concrete and the nonlinear behavior from interfacial separation, crushing of concrete, and yielding of steel. Structural sensitivity analyses are performed with respect to the coefficient of lateral ground pressure. The influence of creep of concrete at unreinforced interfaces on the overall structural behavior is demonstrated, based on the interface models by Gladwell and Janßen. Furthermore, the elastic limits and the bearing capacities of segmental tunnel rings are quantified both for unreinforced and bolted interfaces. The corresponding interface law is based on the Bernoulli-Euler hypothesis and on linear-elastic and ideal-plastic behavior of both concrete and steel. In order to underline the reliability of the computed bearing capacities, a bearing-capacity test on a real-scale segmental tunnel ring is re-analyzed. It is concluded that (i) creep of concrete at the interfaces results in an increase of the structural displacements, while the distributions of the inner forces remain practically the same, (ii) interfacial bolts improve the serviceability of segmental tunnel rings, because they ensure the position stability of the lining, and (iii) the bearing capacity of segmental tunnel rings subjected to ground pressure can be estimated reliably, based on the combination of realistic interface models and analytical solutions of the linear theory of slender circular arches.

1. Introduction

During construction and service, segmental tunnel linings must withstand different types of loading. During excavation, the tunnel boring machine creates thrust by pushing hydraulic cylinders against the already completed part of the lining. The resulting *axial* loading of the tunnel lining calls, in the context of structural analysis, for three-dimensional Finite Element simulations (Kasper and Meschke, 2004). After installation of the lining, the annular gap between the ground mass and the lining is filled with cementitious mortar, in order to minimize soil settlements (Fargnoli et al., 2013). During injection, the grouting pressure results in a considerable *radial* loading (Ding et al., 2004; Kasper and Meschke, 2006; Kavvadas et al., 2017). In shallow tunneling, the grouting pressure might be even twice as large as the earth pressure (Han et al., 2017). As the mortar hardens progressively, the radial loading of segmental tunnel linings evolves with time (Ninić

and Meschke, 2017). In addition, the time-dependent behavior of the ground mass and of the concrete have a significant influence on the loading acting on segmental tunnel rings. Long-term stress relaxation of concrete reduces the axial forces of segmental tunnel linings significantly (Arnau et al., 2012). Creep of the ground mass eventually leads to a ground pressure distribution very similar to the initial in-situ stress state (Lee et al., 1999). In the resulting scenario of small axial forces and, thus, dominating radial loading, the failure of segmental tunnel rings is strongly influenced by the failure of the segment-to-segment interfaces (Luttikholt, 2007; Luttikholt et al., 2008), see Fig. 1. This sets the scene for the present paper which aims at studying the influence of interfacial joints on the structural behavior of segmental tunnel linings. The investigation is not only concerned with the bearing capacity of segmental tunnel linings, but also with regular long-term service conditions, including creep of concrete at segment-to-segment interfaces.
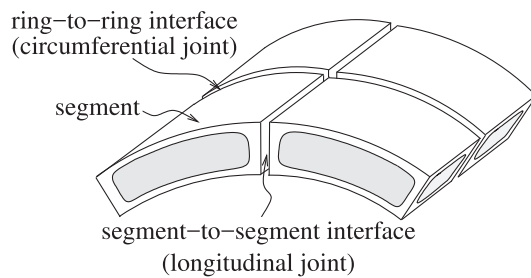

Fig. 1. Segment-to-segment interfaces (also referred to as "longitudinal joints") and ring-to-ring interfaces (also referred to as "circumferential joints").

In some loading scenarios, it is important to consider the interaction between neighboring tunnel rings. One example is large axial loading (Galván et al., 2017), particularly in case of tunnel rings with imperfectly arranged segments (Blom et al., 1999) and/or in case of tunnel linings with misaligned longitudinal joints of neighboring rings (Do et al., 2014; Liu et al., 2018). Another example is partial transfer of dead load from newly installed segments to the already stabilized neighboring ring of segments (Winkler et al., 2004). Significant ring-to-ring interaction is also activated by ground pressure, which varies significantly in the axial direction (Wang et al., 2014), as is encountered in the context of localized radial loading (Arnau and Molins, 2012, 2015). Vice versa, in case of (i) small axial loading, (ii) radial loading which is almost uniform in the longitudinal direction, and (iii) neighboring rings with aligned longitudinal joints, it is reasonable to restrict the investigation to the analysis of single tunnel rings. This is the scenario investigated in the present paper.

Available analytical models for structural analysis of tunnel rings are typically focusing on ground pressure. Initially, such models were simply based on closed rings, without explicit consideration of segment-to-segment interfaces (Morgan, 1961; Muir Wood, 1975). Due to its simplicity, the approach became so popular that it was extended towards consideration of earthquake loads (Penzien and Wu, 1998). In addition, many efforts were made in order to provide "correction factors" for tunnel rings consisting of a specific number of segments and a specific arrangement of interfacial joints (Lee and Ge, 2001). Finally, segment-to-segment interfaces were explicitly considered, based on an interface law in the form of a linear relation between the bending moment and the relative rotation angle and on the assumption that the relative rotation angles at the joints result in rigid body motions of the segments (El Naggar and Hinchberger, 2008). The present paper is a continuation of this line of research, based on consideration of either *time-dependent* or *nonlinear* interface behavior.

The structural behavior of individual segmental tunnel rings is particularly sensitive to relative rotation angles (but significantly less sensitive to radial and circumferential dislocations) developing at segment-to-segment interfaces (Do et al., 2013). The relative rotation angles are nonlinear functions of the bending moments and the normal forces, which are transmitted across the interfaces. Classical interface models were developed by Gladwell (1980) and Janßen (1983). Both models are based on the assumption of *linear* material behavior of concrete. Nonetheless, both models are *nonlinear,* because they are capable of describing loss of full-face segment-to-segment contact, resulting in partial segment-from-segment separation. Materially nonlinear interface models were derived in the context of combined experimental-computational approaches, see, e.g., (Tvede-Jensen et al., 2017; Caratelli et al., 2018) for unreinforced interfaces, and (Li et al., 2015; Liu et al., 2017) for bolted interfaces. Different structural layouts of segment-to-segment interfaces were analyzed in detail (Majdi et al., 2016), and the benefits resulting from the replacement of traditional concrete by steel-fiber reinforced concrete were demonstrated (Gong et al., 2017).

The present paper aims at quantifying the influence of the *local* behavior of segment-to-segment interfaces on the *overall* structural behavior of segmental tunnel rings subjected to ground pressure. To this end, *time-dependent* and *nonlinear* interface models are combined with *linear* "transfer relations", representing analytical solutions of the governing equations of the linear theory of slender circular arches (Zhang et al., 2017). This modeling approach (i) supports a predominantly analytical mode of structural analysis and (ii) limits, to the greatest possible extent, numerical and iterative solutions of nonlinear subproblems.

As for structural analyses, a tunnel ring, consisting of six reinforced concrete segments, is studied. Structural sensitivity analyses are carried out with respect to the coefficient of lateral ground pressure, K. Starting from isotropic loading ($K = 1$), the value of K is progressively decreased down to $K = 0.5$. Three types of structural sensitivity analyses are performed in order to study (i) the influence of *creep* of concrete in the interfacial regions on the overall behavior of the investigated segmental tunnel ring, (ii) the intensity of the ground pressure related to the *elastic limit* of the segmental tunnel ring, and (iii) the intensity of the ground pressure related to the *bearing capacity* of the segmental tunnel ring.

The first type of structural sensitivity analysis refers to unreinforced interfaces. The role of creep of concrete in the interfacial regions is studied, based on the interface models by Gladwell and Janßen. Gladwell's model rests on linear-elastic behavior of concrete. The theoretical basis of Janßen's model, in turn, are recommendations for the design of unreinforced concrete hinges, which were developed in the field of integral bridge construction by Leonhardt and Reimann (1965). They assumed that the *total* compliance of concrete, related to its elastic *and* creep deformation, is twice as large as the elastic compliance, see also (Schlappal et al., 2017). Along this line of reasoning, Janßen's model can be used to account for creep of unreinforced interfaces, albeit in a simplified manner. Finally, Janßen's model is extended, in the sense of a first approach, towards consideration of long-term creep of concrete. The resulting *time-dependent* interface model is used for quantifying the long-term evolution of the ovalization of the cross-section of a segmental tunnel lining, following from creep of concrete at interfaces during regular structural service.

The other two types of structural sensitivity analysis refer to the determination of the elastic limit and the bearing capacity of a segmental tunnel ring, subjected to ground pressure. Analyzing two similar tunnel rings, one with unreinforced interfaces and the other with bolted interfaces, allows for studying the influence of interfacial steel bolts on the overall structural behavior of a segmental tunnel ring. In order to assess the reliability of the model-predicted bearing capacity, a real-scale test on a segmental tunnel ring with bolted interfaces (Liu et al., 2016) is re-analyzed. In the respective test, the structure was loaded by point loads, simulating anisotropic ground pressure. After a proportional load increase, the vertical loading was held constant and the lateral loading was progressively reduced, until the bearing capacity was reached.

The paper is structured as follows. Section 2 provides a brief overview over the transfer relations employed for structural analysis of segmental tunnel rings. Section 3 refers to the interface models. The models by Gladwell and Janßen are briefly described. A model for nonlinear material behavior of concrete and steel is derived, and its predictive capability is assessed quantitatively. In Section 4, the transfer relations are combined with the interface models in the framework of structural sensitivity analysis. Interfacial creep, elastic limits, and bearing capacities of segmental tunnel rings are studied as a function of the coefficient of lateral ground pressure. Section 5 is devoted to the assessment of the reliability of the model-predicted bearing capacities. Section 6 contains the conclusions drawn from the results of the presented analyses.

2. Structural analysis of segmental tunnel rings using transfer relations

2.1. Transfer relations

Structural analysis of segmental tunnel rings may be based on transfer relations, representing analytical solutions of the governing equations of the linear theory of slender circular arches (Zhang et al., 2017). These equations read as (Zhang et al., 2017)

$$\theta = \frac{1}{R}\frac{du}{d\varphi} - \frac{v}{R}, \tag{1}$$

$$N = EA\left(\frac{u}{R} + \frac{1}{R}\frac{dv}{d\varphi}\right), \tag{2}$$

$$M = -EI\left(\frac{1}{R^2}\frac{d^2u}{d\varphi^2} - \frac{1}{R^2}\frac{dv}{d\varphi}\right), \tag{3}$$

$$-\frac{N}{R} + \frac{1}{R}\frac{dV}{d\varphi} + q_r = 0, \tag{4}$$

$$\frac{1}{R}\frac{dN}{d\varphi} + \frac{V}{R} + q_\varphi = 0, \tag{5}$$

$$\frac{1}{R}\frac{dM}{d\varphi} = V. \tag{6}$$

In Eqs. (1)–(6), R, EA, and EI denote the radius of the axis of the arch, the extensional stiffness, and the bending stiffness, respectively. Further, φ denotes the circumferential coordinate, θ stands for the cross-sectional rotation, u and v denote the radial and the circumferential displacement, respectively, N, M, and V stand for the axial force, the bending moment, and the shear force, respectively, q_r and q_φ denote the distributed external loading in the radial direction and in the circumferential direction, respectively. The analytical solution of Eqs. (1)–(6) is cast into a matrix-vector representation, introduced by Rubin and Vogel (1993), representing "transfer relations". They read as (Zhang et al., 2017)

$$\begin{bmatrix} u(\varphi) \\ v(\varphi) \\ \theta(\varphi) \\ M(\varphi) \\ N(\varphi) \\ V(\varphi) \\ 1 \end{bmatrix} = \begin{bmatrix} \cos\varphi & \sin\varphi & T_{13}(\varphi) & T_{14}(\varphi) & T_{15}(\varphi) & T_{16}(\varphi) & \sum u^L(\varphi) \\ -\sin\varphi & \cos\varphi & T_{23}(\varphi) & T_{24}(\varphi) & T_{25}(\varphi) & T_{26}(\varphi) & \sum v^L(\varphi) \\ 0 & 0 & 1 & T_{34}(\varphi) & T_{35}(\varphi) & T_{36}(\varphi) & \sum \theta^L(\varphi) \\ 0 & 0 & 0 & 1 & T_{45}(\varphi) & T_{46}(\varphi) & \sum M^L(\varphi) \\ 0 & 0 & 0 & 0 & \cos\varphi & -\sin\varphi & \sum N^L(\varphi) \\ 0 & 0 & 0 & 0 & \sin\varphi & \cos\varphi & \sum V^L(\varphi) \\ 0 & 0 & 0 & 0 & 0 & 0 & 1 \end{bmatrix} \begin{bmatrix} u_i \\ v_i \\ \theta_i \\ M_i \\ N_i \\ V_i \\ 1 \end{bmatrix}. \tag{7}$$

The components T_{13} to T_{46} of the transfer matrix read as (Zhang et al., 2017)

$$T_{13}(\varphi) = R\sin\varphi, \qquad T_{14}(\varphi) = \frac{R^2}{EI}(\cos\varphi - 1),$$

$$T_{15}(\varphi) = \frac{R}{EA}\frac{1}{2}\varphi\sin\varphi + \frac{R^3}{EI}\left(\frac{1}{2}\varphi\sin\varphi + \cos\varphi - 1\right),$$

$$T_{16}(\varphi) = \frac{R}{EA}\left(\frac{1}{2}\varphi\cos\varphi - \frac{1}{2}\sin\varphi\right) + \frac{R^3}{EI}\left(\frac{1}{2}\varphi\cos\varphi - \frac{1}{2}\sin\varphi\right),$$

$$T_{23}(\varphi) = R(\cos\varphi - 1), \qquad T_{24}(\varphi) = \frac{R^2}{EI}(\varphi - \sin\varphi),$$

$$T_{25}(\varphi) = \frac{R}{EA}\left(\frac{1}{2}\varphi\cos\varphi + \frac{1}{2}\sin\varphi\right) + \frac{R^3}{EI}\left(\varphi - \frac{3}{2}\sin\varphi + \frac{1}{2}\varphi\cos\varphi\right),$$

$$T_{26}(\varphi) = \frac{R}{EA}\left(-\frac{1}{2}\varphi\sin\varphi\right) + \frac{R^3}{EI}\left(1 - \cos\varphi - \frac{1}{2}\varphi\sin\varphi\right),$$

$$T_{34}(\varphi) = -\frac{R}{EI}\varphi, \qquad T_{35}(\varphi) = \frac{R^2}{EI}(\sin\varphi - \varphi),$$

$$T_{36}(\varphi) = \frac{R^2}{EI}(\cos\varphi - 1),$$

$$T_{45}(\varphi) = R(1 - \cos\varphi), \qquad T_{46}(\varphi) = R\sin\varphi. \tag{8}$$

The vector on the left-hand-side of Eq. (7) contains the six kinematic

and static variables, referring to the cross-section at an arbitrary value of the angular coordinate φ. The vector on the right-hand-side of Eq. (7) contains six integration constants. They represent six kinematic and static variables, referring to the initial cross-section (index "i"), i.e. to the circumferential position $\varphi = 0$. The top-left six-by-six submatrix of the transfer matrix in Eq. (7) refers to the solution for an unloaded segmental tunnel ring (Zhang et al., 2017). The summation symbols in the last column of the transfer matrix in Eq. (7) refer to the superposition of so-called "load integrals". The latter represent analytical solutions for (i) the relative rotation angles at segment-to-segment interfaces, (ii) the ground pressure, and (iii) radial point loads.

2.2. Analytical solutions for relative rotation angles

The load integrals for a relative rotation angle, $\Delta\theta_j$, at the interface $\varphi = \varphi_j$, read as (Zhang et al., 2017)

$$u^L(\varphi) = -R\Delta\theta_j\sin(\varphi - \varphi_j)H(\varphi - \varphi_j), \tag{9}$$

$$v^L(\varphi) = R\Delta\theta_j[1 - \cos(\varphi - \varphi_j)]H(\varphi - \varphi_j), \tag{10}$$

$$\theta^L(\varphi) = \Delta\theta_j H(\varphi - \varphi_j), \tag{11}$$

$$N^L(\varphi) = V^L(\varphi) = M^L(\varphi) = 0, \tag{12}$$

where $H(\varphi - \varphi_j)$ stands for the Heaviside function.

2.3. Analytical solution for the ground pressure

The vertical and the horizontal component of the ground pressure are denoted as σ_v and σ_h, respectively, see Fig. 2(a). At any circumferential position φ along the external boundary of the segmental tunnel ring, the principal normal stresses σ_v and σ_h are transformed into radial normal stresses σ_{rr} and shear stresses $\sigma_{r\varphi}$, using the transformation equations for plane stress states (Young and Budynas, 2002), see Fig. 2(a). The resulting expressions for σ_{rr} and $\sigma_{r\varphi}$ are multiplied by the axial length of the segments, B, delivering the distributed line loads q_r and q_φ acting on the segmental ring as

$$q_r = -B\left(\frac{\sigma_v + \sigma_h}{2} + \frac{\sigma_v - \sigma_h}{2}\cos2\varphi\right), \tag{13}$$

$$q_\varphi = B\left(\frac{\sigma_v - \sigma_h}{2}\sin2\varphi\right), \tag{14}$$

see also Fig. 2(b) and (c).

The load integrals for the ground pressure are obtained by specifying Eqs. (1)–(6) for Eqs. (13) and (14), by following the step-by-step integration strategy described in (Zhang et al., 2017), and by considering homogeneous initial conditions. They read as

$$N^L(\varphi) = \frac{BR}{6}[\sigma_v(-\cos2\varphi + 4\cos\varphi - 3) + \sigma_h(\cos2\varphi + 2\cos\varphi - 3)], \tag{15}$$

$$V^L(\varphi) = \frac{BR\sin\varphi}{3}[\sigma_v(\cos\varphi + 2) + \sigma_h(1 - \cos\varphi)], \tag{16}$$

$$M^L(\varphi) = \frac{BR^2}{6}(\cos\varphi - 1)[\sigma_v(-\cos\varphi - 5) + \sigma_h(\cos\varphi - 1)], \tag{17}$$

$$\begin{aligned} u^L(\varphi) = {}& \frac{BR^4}{18EI}[\sigma_v(-\cos^2\varphi + 6\varphi\sin\varphi + 14\cos\varphi - 13) \\ & + \sigma_h(\cos^2\varphi + 3\varphi\sin\varphi + 4\cos\varphi - 5)] \\ & + \frac{BR^2}{18EA}[\sigma_v(2\cos^2\varphi + 6\varphi\sin\varphi + 8\cos\varphi - 10) \\ & + \sigma_h(-2\cos^2\varphi + 3\varphi\sin\varphi + 10\cos\varphi - 8)], \end{aligned} \tag{18}$$
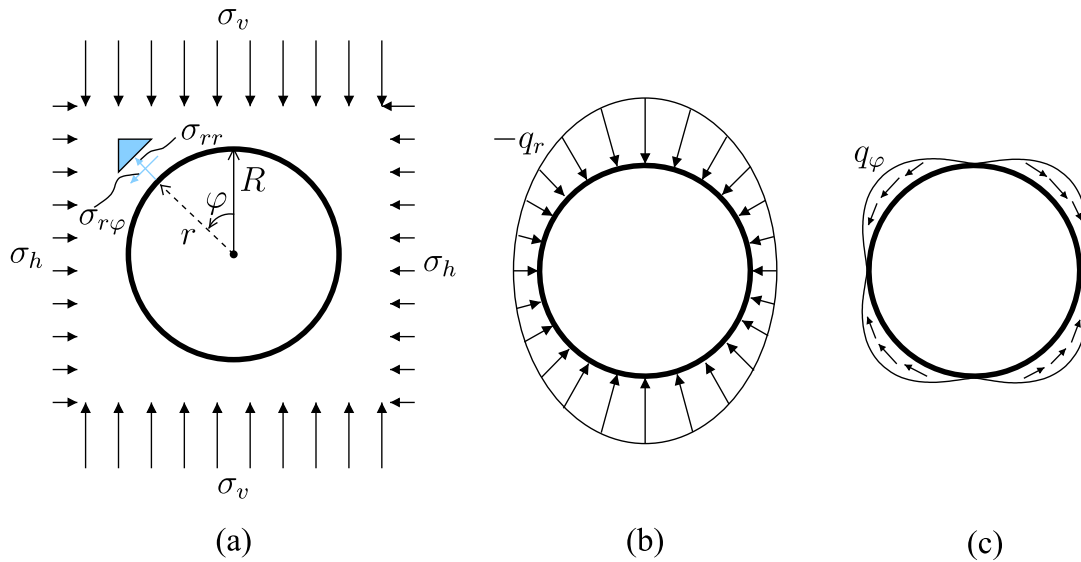
Fig. 2. Decomposition of ground pressure into radial and circumferential components: (a) vertical ground pressure σ_v and lateral ground pressure σ_h, (b) distribution of the radial loading, q_r, and (c) distribution of the circumferential loading, q_φ; r and φ denote the coordinates of the polar coordinate system and R stands for radius of the axis of the segmental tunnel ring.

$$
\begin{aligned}
v^L(\varphi) =\ & \frac{BR^4}{36EI}[\sigma_v(\cos\varphi\sin\varphi + 12\varphi\cos\varphi - 40\sin\varphi + 27\varphi) \\
& + \sigma_h(-\cos\varphi\sin\varphi + 6\varphi\cos\varphi - 14\sin\varphi + 9\varphi)] \\
& + \frac{BR^2}{36EA}[\sigma_v(-8\cos\varphi\sin\varphi + 12\varphi\cos\varphi - 4\sin\varphi) \\
& + \sigma_h(8\cos\varphi\sin\varphi + 6\varphi\cos\varphi - 14\sin\varphi)],
\end{aligned}
\tag{19}
$$

$$
\begin{aligned}
\theta^L(\varphi) =\ & \frac{BR^3}{12EI}[\sigma_v(\cos\varphi\sin\varphi + 8\sin\varphi - 9\varphi) \\
& + \sigma_h(-\cos\varphi\sin\varphi + 4\sin\varphi - 3\varphi)].
\end{aligned}
\tag{20}
$$

2.4. Analytical solutions for radial point loads

For validation purposes, a real-scale test will be analyzed, in which a segmental tunnel ring was subjected to radial point loads. The load integrals for a radial point load P, acting at position φ_p, read as (Zhang et al., 2017):

$$
u^L(\varphi) = \frac{1}{2}\left(\frac{PR}{EA} + \frac{PR^3}{EI}\right)[\sin(\varphi - \varphi_p) - (\varphi - \varphi_p)\cos(\varphi - \varphi_p)]H(\varphi - \varphi_p),
\tag{21}
$$

$$
\begin{aligned}
v^L(\varphi) =\ & \frac{PR}{EA}\left[\frac{1}{2}(\varphi - \varphi_p)\sin(\varphi - \varphi_p)\right]H(\varphi - \varphi_p) \\
& + \frac{PR^3}{EI}\left[\frac{1}{2}(\varphi - \varphi_p)\sin(\varphi - \varphi_p) + \cos(\varphi - \varphi_p) - 1\right]H(\varphi - \varphi_p),
\end{aligned}
\tag{22}
$$

$$
\theta^L(\varphi) = \frac{PR^2}{EI}[1 - \cos(\varphi - \varphi_p)]H(\varphi - \varphi_p),
\tag{23}
$$

$$
M^L(\varphi) = -R\,P\sin(\varphi - \varphi_p)H(\varphi - \varphi_p),
\tag{24}
$$

$$
N^L(\varphi) = P\sin(\varphi - \varphi_p)H(\varphi - \varphi_p),
\tag{25}
$$

$$
V^L(\varphi) = -P\cos(\varphi - \varphi_p)H(\varphi - \varphi_p).
\tag{26}
$$

2.5. Identification of integration constants

The six integration constants u_i, v_i, θ_i, M_i, N_i, and V_i, forming the vector of state variables on the right-hand-side of Eq. (7), are identified

as follows. The kinematic variables u_i, v_i, and θ_i refer to a rigid body motion of the segmental tunnel ring (Zhang et al., 2017). Without loss of generality, it may be set equal to zero

$$
u_i = v_i = \theta_i = 0.
\tag{27}
$$

As for the identification of the three static variables M_i, N_i, and V_i, three geometric continuity conditions are formulated for the *closed* segmental tunnel ring (Zhang et al., 2017). To this end, the transfer relations are specified for $\varphi = 2\pi$, resulting in a relation between the state variables at the initial and the final (index "f") cross-section. Since the final cross-section is equal to the initial cross-section, the geometric compatibility conditions are obtained as $u_f = u_i$, $v_f = v_i$, and $\theta_f = \theta_i$. This delivers three linear equations for M_i, N_i, and V_i. Their solutions read as

$$
\begin{aligned}
M_i =\ & \frac{EI}{2R\pi(EA\,R^2 + EI)}\left[2EA\,R\sum v^L(2\pi)\right. \\
& \left. + (3EA\,R^2 + EI)\sum \theta^L(2\pi)\right],
\end{aligned}
\tag{28}
$$

$$
N_i = -\frac{EI\,EA}{R\pi(EA\,R^2 + EI)}\left[\sum v^L(2\pi) + R\sum \theta^L(2\pi)\right],
\tag{29}
$$

$$
V_i = -\frac{EI\,EA}{R\pi(EA\,R^2 + EI)}\sum u^L(2\pi).
\tag{30}
$$

Eqs. (7)–(30) render an analytical structural analysis of segmental tunnel rings possible, provided that (i) material behavior of the segments is linear-elastic, (ii) the external loading is known, and (iii) the relative rotation angles at the interfaces were *measured*, see, e.g., the re-analysis of a real-scale test, documented in (Zhang et al., 2017). If the relative rotation angles are *unknown*, interface models are needed to compute them.

3. Interface models

Interface models provide mathematical expressions for relative rotation angles at segment-to-segment interfaces, $\Delta\theta$, as functions of the bending moment M and the compressive normal force N, transmitted across these interfaces. Thereby, the ratio between the bending moment and the normal force is referred to as the eccentricity e of the interface:

$$e = \frac{M}{|N|}. \tag{31}$$

Small eccentricities indicate full-face contact between neighboring segments, while larger eccentricities result in partial segment-from-segment separation.

3.1. Interface model by Gladwell (1980)

The interface model by Gladwell (1980) refers to the elastic contact problem of a rectangular flat punch, pressed unsymmetrically into a half space. The surface of the punch, exhibiting the width b and the height h, is equal to the initial interfacial contact area between two neighboring segments.

Gladwell's model describes full-face contact between neighboring segments for eccentricities $|e| \leqslant h/4$. The corresponding relative rotation angles increase linearly with increasing bending moment, and they are independent of the eccentricity (Gladwell, 1980)

$$\Delta\theta = \frac{32\,(1 - \nu_c^2)}{\pi\,E_c\,b\,h^2}\,M, \qquad |e| \leqslant h/4, \tag{32}$$

where E_c and ν_c denote Young's modulus and Poisson's ratio of plain concrete.

Gladwell's model describes segment-from-segment separation for eccentricities in the interval $h/4 < |e| < h/2$. The corresponding relative rotation angles increase linearly with increasing bending moment and nonlinearly with increasing eccentricity (Gladwell, 1980)

$$\Delta\theta = \frac{32\,(1 - \nu_c^2)}{\pi\,E_c\,b\,h^2 \left(\frac{4\,e}{h}\right)^2 \left(\frac{h}{2\,|e|} - 1\right)}\,M, \qquad h/4 \leqslant |e| \leqslant h/2. \tag{33}$$

According to Eq. (33), the relative rotation angle tends to infinity as the eccentricity approaches the maximum value, $h/2$,

$$e \to \pm h/2 \quad \Rightarrow \quad \Delta\theta \to \pm\infty. \tag{34}$$

see also Fig. 3(a).

3.2. Interface model by Janßen (1983)

The interface model by Janßen (1983) is based on design formulae for unreinforced concrete hinges by Leonhardt and Reimann (1965). The latter were derived, based on linear distributions of the compressive stresses in the contact region.

Janßen's model describes full-face contact between neighboring segments for eccentricities $|e| \leqslant h/6$. The corresponding relative rotation angles increase linearly with increasing bending moment, and they are independent of the eccentricity (Janßen, 1983)

$$\Delta\theta = \frac{12}{E_c\,b\,h^2}\,M, \qquad |e| \leqslant h/6. \tag{35}$$

Janßen's model describes segment-from-segment separation for eccentricities in the interval $h/6 < |e| < h/2$. The corresponding relative rotation angle increases linearly with increasing bending moment and nonlinearly with increasing eccentricity (Janßen, 1983)

$$\Delta\theta = \frac{12}{E_c\,b\,h^2\,\frac{27|e|}{2h}\left(1 - \frac{2|e|}{h}\right)^2}\,M, \qquad h/6 \leqslant |e| \leqslant h/2, \tag{36}$$

see Fig. 3(b). Again, the relative rotation angle tends to infinity as the eccentricity approaches $h/2$, see Eq. (34).

3.3. Nonlinear model for bolted interfaces, considering linear-elastic and ideal-plastic material behavior of concrete and steel

Inspired by the available interface models, see, e.g., (Li et al., 2015; Liu et al., 2017; Tvede-Jensen et al., 2017; Caratelli et al., 2018), a nonlinear interface model is developed for bolted segment-to-segment interfaces, see Fig. 4(a). Linear-elastic and ideal-plastic material behavior is assumed for both steel and concrete, see Fig. 5, where E_c and E_s denote Young's moduli and Ff_c and f_y stand for the elastic-limits of concrete and steel, respectively. Actually, f_y is the yield stress of steel, f_c the uniaxial compressive strength of the concrete, and F is a strength-increase-factor, to be explained in the following paragraph. Before that, it is emphasized that the concrete only transmits compressive stresses across the interface. The transmission of tensile stresses is impossible, because of separation of the two segments. The steel bolt, in turn, transmits only tensile forces across the interface, because it is fixed by screws at both ends. Separation of these screws from the surrounding concrete prevents the development of compressive forces in the bolt, see Fig. 4(a).

Concrete is linear-elastic up to a stress level that is F-times *larger* than the uniaxial compressive strength f_c, see Fig. 5(a). The modeling approach is motivated by the findings of Kalliauer et al. (2017), who simulated reinforced concrete hinges, subjected to eccentric compression. By analogy to reinforced concrete hinges, also segment-to-segment interfaces represent necks in reinforced concrete structures. The stress trajectories must run around these necks. This results in *triaxial* compressive stress states in the interface region. The corresponding confinement pressure results in an increase of the strength of concrete relative to its uniaxial compressive strength. The triaxial-to-uniaxial compressive strength ratio, F, can be estimated reliably on the basis of Eurocode-recommendations for partially loaded areas (Marx and Schacht, 2010; Kalliauer et al., 2017; European Committee for Standardization, 2014):
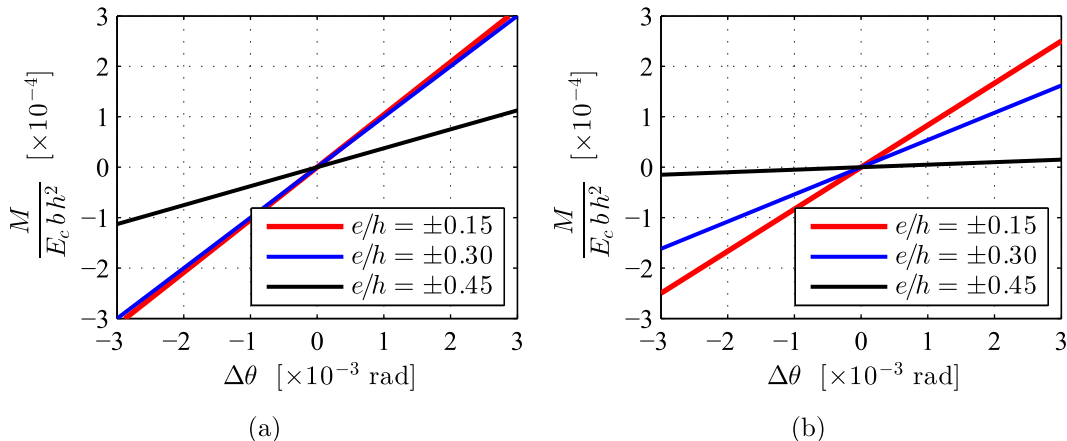

Fig. 3. Interface model of (a) Gladwell (1980); and (b) Janßen (1983): relation between the dimensionless bending moment and the relative rotation angle as a function of the eccentricity e/h.
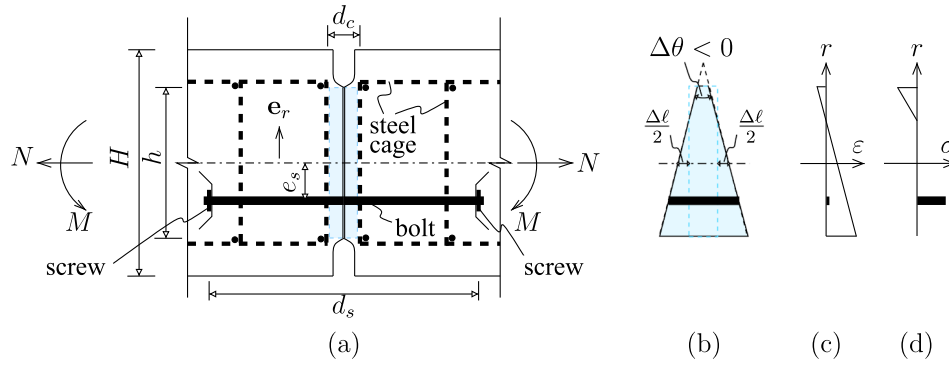
Fig. 4. Interface between two steel-reinforced concrete segments, connected by an eccentrically positioned steel bolt: (a) structural dimensions and directions of positive stress resultants, (b) prescribed deformation of the interface region, (c) strain distribution, and (d) stress distribution.
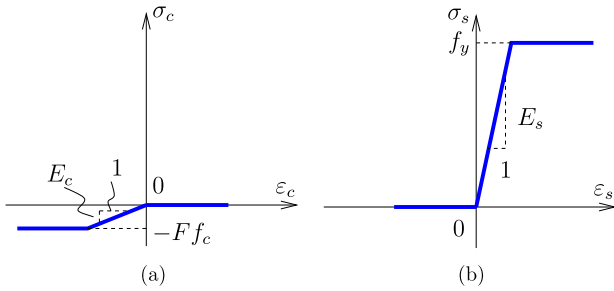

Fig. 5. Linear-elastic and ideal-plastic material behavior of (a) concrete and (b) steel; σ_c, ε_c, E_c, f_c, and F, denote the normal stress, the normal strain, Young's modulus, the uniaxial compressive strength, and the triaxial-to-uniaxial strength ratio of concrete, respectively, while σ_s, ε_s, E_s, and f_y stand for the normal stress, the normal strain, Young's modulus, and the yield strength of steel, respectively.

$$F = \sqrt{\frac{3\,B}{b}}, \tag{37}$$

where B and b denote the width of partially loaded areas and of the "maximum" distribution area, respectively. Herein, they are equal to the width of the segment and of the interface, respectively.

Modeling of *ideal-plastic* compressive failure of concrete, see Fig. 5(a), is also motivated by the findings of Kalliauer et al. (2017). They performed three-dimensional Finite Element simulations of bearing-capacity tests on concrete hinges subjected to eccentric compression. The simulation results have shown that the ductile *structural* failure of concrete hinges is a consequence of the surprisingly ductile *material* failure of concrete subjected to compressive multiaxial stresses.

The mathematical formulation of the nonlinear interface model is derived under the assumption that segment-to-segment interfaces are subjected, in a displacement-controlled fashion, to an axial shortening $\Delta\ell$ and to a relative rotation angle $\Delta\theta$, see Fig. 4(b). In the following, corresponding expressions for the normal force N and the bending moment M are derived. Following Leonhardt and Reimann's approach, this derivation is based on the Bernoulli-Euler hypothesis. In other words, it is assumed that all cross-sections in the interface region remain plane at any time. This results in a linear distribution of the axial strains along the height of the interface, which is resolved by the radial coordinate r

$$\varepsilon_c(r) = \frac{\Delta\ell}{d_c} + \frac{\Delta\theta}{d_c}(r - R), \tag{38}$$

see Fig. 4(c). In Eq. (38), d_c denotes the effective length of the interface, which is equal to the distance of the reinforcement cages of the two connected segments, see Fig. 4(a). The steel bolts run across the interface. They are tightened by screws at both ends. The length of the bolts is equal to the screw-to-screw distance, denoted as d_s, see Fig. 4(a). As for the

quantification of the axial strain of the bolts, ε_s, the change of length of the bolts, $\Delta\ell_s$, is set equal to the change of length of the surrounding concrete, $\Delta\ell_c(r_s)$, where r_s denotes the radial coordinate of the bolts:

$$\Delta\ell_s = d_s\,\varepsilon_s = d_c\,\varepsilon_c(r_s) = \Delta\ell_c(r_s) \quad \Rightarrow \quad \varepsilon_s = \frac{d_c}{d_s}\,\varepsilon_c(r_s). \tag{39}$$

The axial normal stresses of the concrete and the steel follow from inserting the strains (38) and (39) into the constitutive laws illustrated in Fig. 5. This results (i) in a linear (or bilinear) distribution of compressive normal stresses of concrete, in the contact region of the segment-to-segment interface, where compressive strains of concrete prevail, i.e. $\varepsilon_c(r) < 0$, and (ii) in a constant stress of the bolts, see Fig. 4(d). Finally, the stress resultants M and N follow from the standard relations (Zhang et al., 2017)

$$M = \int_A \sigma\cdot(r - R)\mathrm{d}A \tag{40}$$

and

$$N = \int_A \sigma\mathrm{d}A. \tag{41}$$

The expressions for M and N are available in Appendix C. Full-face segment-to-segment contact is described for eccentricities $|e| \leqslant h/6$, by analogy to Leonhardt and Reimann's approach. The bolts are not active ($\sigma_s = 0$) and the normal stresses of concrete simply read as $\sigma_c = E_c\,\varepsilon_c$, with ε_c according to Eq. (38). Inserting the stress state into Eq. (40) delivers the following linear relation between M and $\Delta\theta$

$$\Delta\theta = \frac{12\,d_c}{E_c\,b\,h^3}\cdot M, \qquad |e| \leqslant h/6. \tag{42}$$

Once the eccentricity increases such that segment-from-segment separation takes place, the nonlinear interface model is evaluated numerically as follows. Eqs. (38)–(41) are combined with the constitutive laws illustrated in Fig. 5. This establishes a relation between the prescribed input values of $\Delta\ell$ and $\Delta\theta$, on the one hand, and the stress resultants M and N, on the other hand. Many different combinations of $\Delta\ell$ and $\Delta\theta$ are used as input in order to compute corresponding values of M and N. Input and output values are stored in look-up tables. As for the simulation of *load-controlled tests*, pairs of values of N and M are used as input for these tables in order to determine the corresponding value of the sought relative rotation angle.

In order to demonstrate the performance of the nonlinear interface model, it is employed for simulation of the structural behavior of a bolted interface subjected to eccentric compression right up to its load-carrying capacity. The relevant geometric and material properties of the studied interface are listed in Table 1. Since the bolts are positioned at a distance e_s below the centerline of the interface, see Fig. 4(a), the moment-rotation relation of the interface depends on the sign of the applied bending moment. A negative bending moment leads to a larger bearing capacity of the interface, compared to a positive bending moment (see Fig. 4(a) for the definition of a positive bending moment).

Table 1
Properties of the bolted interfaces tested by Liu et al. (2017).

|	
width of the segments	$B = 1.2$ m
height of the segments	$H = 0.35$ m
radius of the segmental tunnel ring	$R = 2.93$ m
width of the interface	$b = 1.0$ m
height of the interface	$h = 0.24$ m
effective length of the interface	$d_c = 0.06$ m
eccentricity of the bolts	$e_s = 5.5$ cm
diameter of the bolts	$D_s = 30$ mm
length of the bolts	$d_s = 0.40$ m
number of bolts at each interface	$N_s = 2$
Young's modulus of the bolts	$E_s = 200$ GPa
yield stress of the bolts	$f_y = 500$ MPa
Young's modulus of concrete	$E_c = 43.6$ GPa
Poisson's ratio of concrete	$\nu_c = 0.24$
uniaxial compressive strength of concrete	$f_c = 35.5$ MPa
triaxial-to-uniaxial compressive strength ratio of concrete[a]	$F = 1.90$

[a] Following from Eq. (37).
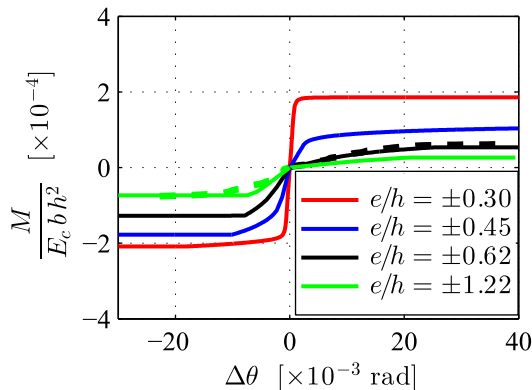
Fig. 6. Performance of the nonlinear interface model considering linear-elastic and ideal-plastic behavior of both concrete and steel, see the solid lines, and experimental data from Liu et al. (2017), see the dashed lines.

This expected behavior is reproduced by the results obtained from the simulation of eight different eccentric compression tests, with dimensionless eccentricities, e/h, amounting to $\pm$ 0.30, $\pm$ 0.45, $\pm$ 0.62, $\pm$ 0.62, and $\pm$ 1.22, see the solid lines in Fig. 6.

The nonlinear interface model suggests that the initial stiffness of the bolted interface decreases with increasing eccentricity, because larger eccentricities result in a more pronounced separation of the two connected segments. Still, at small intensities of the compressive loading, the relative rotation angle increases linearly with increasing loading. This linear behavior is related to (i) the constant eccentricity, (ii) the constant segment-to-segment contact area, and (iii) linear-elastic material behavior of both concrete and steel. The nonlinear parts of the graphs in Fig. 6 are the consequence of (i) nonlinear material behavior, i.e. of crushing of the concrete and yielding of the steel, and (ii) changes of the segment-to-segment contact area induced, at constant eccentricity, by the material nonlinearities. Crushing of concrete starts in the outermost region on the compressed side of the interface. Further increase of the loading results in the growth of a "crushing zone", in the direction of the centerline of the interface, by analogy to the growth of "yielding zones" in the theory of plastic hinges. The bearing capacity of the interface is reached asymptotically, once the bolt is yielding and concrete is crushing along the entire contact region between the two connected segments, see the finally approached plateaus in Fig. 6.

The predictive capabilities of the nonlinear interface model are assessed, based on experimental data from Liu et al. (2017). The tested assemblies consisted of two reinforced concrete segments. Loading was
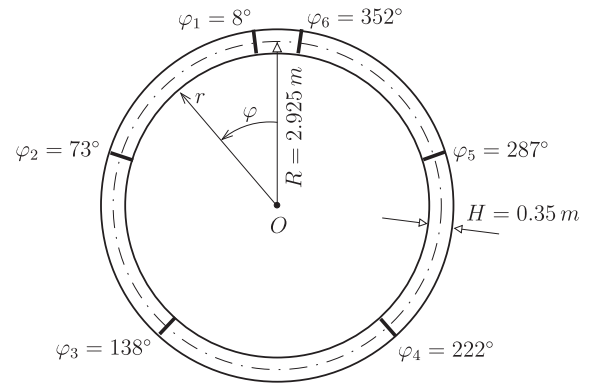

Fig. 7. Cross-section of the analyzed tunnel ring consisting of six segments.

prescribed such that the segment-to-segment interface was subjected to eccentric compression. In the first test the constant dimensionless eccentricity e/h amounted to $+0.62$ and in the second test to -1.22, see the dashed lines in Fig. 6. The model predictions agree well with the experimental data. This corroborates the usefulness of the developed interface model and provides the motivation to employ it for structural simulations of segmental tunnel rings.

4. Combination of transfer relations and interface laws for structural analysis of segmental tunnel rings subjected to ground pressure

The exemplarily analyzed segmental tunnel ring is similar to the structure studied by Zhang et al. (2017). The ring consists of six precast reinforced concrete segments, see Fig. 7. The geometric properties of the structure are listed in Table 1. The angular coordinate φ defines the positions on the ring. The origin of φ is located at the crown (Fig. 7). The six interfaces are located at $\varphi_1 = 8°$, $\varphi_2 = 73°$, $\varphi_3 = 138°$, $\varphi_4 = 222°$, $\varphi_5 = 287°$, and $\varphi_6 = 352°$. The material properties of concrete and steel are listed in Table 1.

As for the structural analysis, the segmental tunnel ring is subjected to ground pressure (Fig. 2). The sensitivity of the structural behavior with respect to the coefficient of lateral ground pressure, K, will be investigated. Thereby, K is defined as the ratio between the horizontal ground pressure and the vertical ground pressure,

$$K = \frac{\sigma_h}{\sigma_v}. \tag{43}$$

The structural problem at hand is symmetric with respect to the vertical axis running through the center of the segmental tunnel ring. Therefore, the six interfaces are grouped into three pairs: two in the crown region, two in the lateral region, and two in the bottom region. The behavior of these interfaces will be modeled, based on the nonlinear interface laws described in Section 3. The segments between the interfaces, in turn, will be modeled, based on the linear transfer relations described in Section 2. The structural analysis requires determination of the relative rotation angles of all three groups of interfaces in a consistent manner with the interface models of Section 3.

4.1. Combined analytical-numerical solution procedure

The starting point of the nonlinear structural analyses are the expressions for the static variables at the crown, see Eqs. (28)–(30). They are inserted into the transfer relations (7). The resulting expression is specified for seven sets of load integrals. One set refers to the known ground pressure, see Eqs. (15)–(20). The other six sets refer to the unknown relative rotation angles at the six interfaces, $\Delta\theta_1$, $\Delta\theta_2$, ..., $\Delta\theta_6$, see Eqs. (9)–(12). Making use of the aforementioned symmetry, $\Delta\theta_6$ is set equal to $\Delta\theta_1$, $\Delta\theta_5$ to $\Delta\theta_2$, and $\Delta\theta_4$ to $\Delta\theta_3$. This reduces the number of

unknowns from six to three. The obtained transfer relations are evaluated for the positions of the three interfaces, $\varphi = \varphi_j$, $j = 1, 2, 3$. The fourth and the fifth line of the evaluated transfer relations deliver the following expressions for the bending moments M_j and the normal forces N_j which are transmitted across the three sets of interfaces, $j = 1, 2, 3$

$$M_j = \frac{EI}{2\pi R(EA\,R^2 + EI)}\left\{2EA\,R\left[\cos\varphi_j \sum v^L(2\pi) - \sin\varphi_j \sum u^L(2\pi)\right]\right.$$
$$\left. + (EAR^2 + EI + 2EAR^2\cos\varphi_j) \sum \theta^L(2\pi)\right\} + \sum M^L(\varphi_j),$$
$$(44)$$

$$N_j = \frac{EA\,EI}{\pi(EA\,R^2 + EI)}[\sin\varphi_j \sum u^L(2\pi) - \cos\varphi_j \sum v^L(2\pi)$$
$$- R\cos\varphi_j \sum \theta^L(2\pi)]$$
$$+ \sum N^L(\varphi_j). \quad (45)$$

The Eqs. (44) and (45) mark the last step of the analytic/symbolic derivation. Consideration of the *nonlinear* interface behavior requires a numerical approach, described next.

The numerical calculation starts with inserting numerical values of R, EA, EI, B, σ_v, and σ_h into the Eqs. (44) and (45). This delivers expressions for M_1, M_2, and M_3 as well as for N_1, N_2, and N_3, which are *linear* functions of the unknown relative rotation angles $\Delta\theta_1$, $\Delta\theta_2$, and $\Delta\theta_3$, i.e.

$$\begin{aligned}
M_1 &= M_1(\Delta\theta_1, \Delta\theta_2, \Delta\theta_3), & N_1 &= N_1(\Delta\theta_1, \Delta\theta_2, \Delta\theta_3),\\
M_2 &= M_2(\Delta\theta_1, \Delta\theta_2, \Delta\theta_3), & N_2 &= N_2(\Delta\theta_1, \Delta\theta_2, \Delta\theta_3),\\
M_3 &= M_3(\Delta\theta_1, \Delta\theta_2, \Delta\theta_3), & N_3 &= N_3(\Delta\theta_1, \Delta\theta_2, \Delta\theta_3).
\end{aligned} \quad (46)$$

First *numerical* estimates of the relative rotation angles are obtained under the assumption of full-face segment-to-segment contact. Depending on the choice of the interface model, the corresponding linear interface law is given either by Eq. (32), or Eq. (35), or Eq. (42). Inserting the expressions for M_1, M_2, and M_3 according to Eq. (46) into the relevant linear interface law, results in a set of three linear equations for the three unknown relative rotation angles. The corresponding solution is straightforward.

In order to check whether or not the assumption of full-face segment-to-segment contact was justified, the numerical values of $\Delta\theta_1$, $\Delta\theta_2$, and $\Delta\theta_3$ are inserted into the expressions (46). The resulting numerical values of M_1 and N_1, M_2 and N_2, as well as M_3 and N_3 allow for quantifying the eccentricities at the three interfaces, see Eq. (31). Provided that the computed eccentricities are small enough such that full-face contact is maintained, the first numerical estimates of $\Delta\theta_1$, $\Delta\theta_2$, and $\Delta\theta_3$ represent the final solution of the structural problem.

If the computed eccentricities imply that at least one of the three pairs of interfaces develops partial segment-from-segment separation, the problem at hand is nonlinear and calls for an iterative determination of the relative rotation angles. The three pairs of computed numerical values of the eccentricities and bending moments are inserted into the respective interface law. This allows for computing improved numerical estimates of the relative rotation angles. They are inserted into Eq. (46), followed by calculation of the eccentricities according to Eq. (31). This procedure is repeated until the eccentricities calculated at the end of two successive iteration steps do not change anymore. The iteration converges quickly.

4.2. Assessment of the role of interfacial creep on the structural behavior of segmental tunnel rings

The following structural sensitivity analysis refers to a comparison of the interface models by Gladwell and Janßen. In both models, linear material behavior of concrete is assumed. The model of Gladwell is based on linear-elastic behavior of concrete. The model of Janßen, in

turn, accounts for a characteristic part of concrete creep, as explained next.

Schlappal et al. (2017) investigated the time-dependent behavior of concrete hinges subjected to sustained eccentric compression. They analyzed the measured evolution of the relative rotation angles, based on the models by Gladwell (1980) and Leonhardt and Reimann (1965). The relative rotation angles, measured right after the end of the loading phase, are reproduced reliably by the linear-elastic model of Gladwell. The model of Leonhardt and Reimann, in turn, describes larger rotation angles, reached some 16 h after the end of the loading phase (Schlappal et al., 2017). This underlines that the model by Leonhardt and Reimann accounts for elastic interface behavior *and* for creep of concrete, developing during short-term structural testing.

With respect to long-term serviceability, Leonhardt and Reimann assumed (i) that creep would asymptotically reach a final value, and (ii) that the finally reached *total* compliance of concrete, related to both instantaneous elastic and delayed creep deformation, would be twice as large as the instantaneous compliance. Therefore, they recommended to divide the elastic stiffness of concrete by a factor of 2. This underlines that the model of Leonhardt and Reimann accounts, albeit in a simplified manner, for creep of concrete hinges. The model of Janßen represents an adaptation of the model of Leonhardt and Reimann for segment-to-segment interfaces used in mechanized tunneling. Dividing the value of Young's modulus of concrete by a factor of 2, and inserting the obtained reduced value into Eqs. (35) and (36) allows for consideration of creep of interfaces in the spirit of Leonhardt and Reimann.

The interface models by Gladwell (1980) and Janßen (1983) are applied to the segmental tunnel ring of Fig. 7. Gladwell's model is evaluated with the realistic value $E_c = 43.6$ GPa, while Janßen's model is evaluated with $E_c = 21.8$ GPa in order to account for the reduced stiffness of interfaces resulting from creep of concrete. The structural behavior under the action of ground pressure with different values of the coefficient of lateral ground pressure is studied. The numerical calculations are carried out as described in Section 4.1. Starting with isotropic loading ($K = 1$), the value of K is progressively decreased.

The interfacial eccentricities are nonlinear functions of K, see Fig. 8. As for isotropic loading ($K = 1$), the interfacial eccentricities vanish. Lowering the value of K, the absolute values of the eccentricities increase particularly at the crown interfaces and the lateral interfaces. Full-face contact is lost at these interfaces for values of K around 0.77 (Gladwell's model) and 0.84 (Janßen's model). Further reduction of K leads to separation also at the bottom interfaces. This is predicted by Gladwell's model for $K = 0.60$, and by Janßen's model for $K = 0.69$. Once K reaches the value 0.54, the interfacial eccentricities predicted by both models grow so large that a kinematic mechanism arises.

The load-carrying behavior of the tunnel ring is illustrated in more detail for $K = 0.722$. This is related to $|e|/h \leq 1/3$ and, thus, to the limit of applicability recommended by Leonhardt and Reimann (1965). This limit refers to the situation that *half* of the initial contact area has got lost. In addition, the vertical ground pressure σ_v is considered to be equal to 1.217 MN/m^2. This corresponds to the elastic limit of the segmental tunnel ring subjected to ground pressure with $K = 0.722$, as will be shown in Section 4.3.

The distributions of the stress resultants M, N, and V, as well as the deformed configuration are evaluated with the transfer relations, see Fig. 9. Based on the identified relative rotation angles, the functions $M(\varphi)$, $N(\varphi)$, and $V(\varphi)$ are obtained by simple evaluation of the transfer relations, see Eq. (7). Both interface models suggest very similar distributions of the inner forces, see Fig. 9(a)–(c). The convergences in the vertical and the horizontal directions, predicted by Janßen's model, are by 61 % and 73 % larger compared to those predicted by Gladwell's model, see Fig. 9(d).

Under long-term loading by constant ground pressure, creep of segment-to-segment interfaces results in an increase of (i) the interfacial eccentricities, see Fig. 8, (ii) the related relative rotation angles, and, thus, (iii) of the structural displacements, see Fig. 9(d). This is the
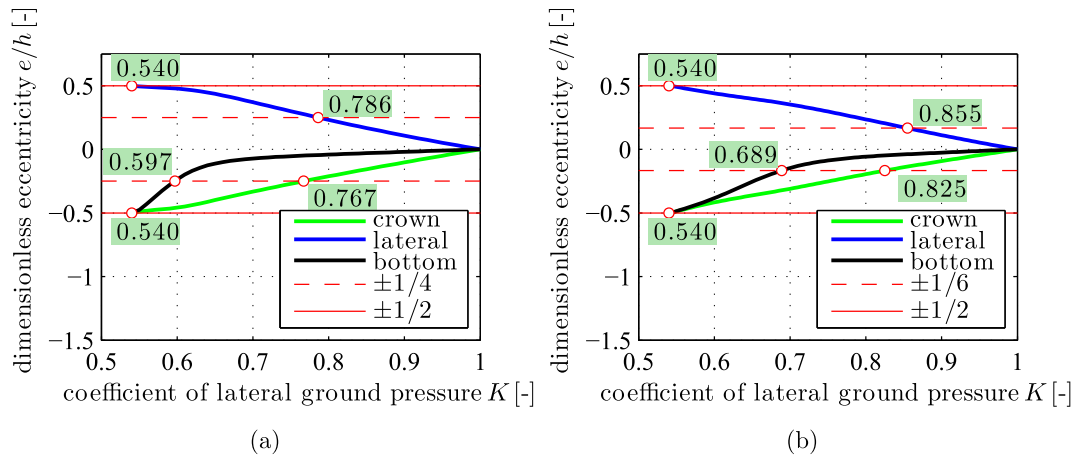
Fig. 8. Interfacial eccentricities as a function of the coefficient of lateral ground pressure: results from structural sensitivity analysis of the segmental tunnel ring of Fig. 7: (a) Gladwell's model evaluated with E_c = 43.6 GPa and (b) Janßen's model evaluated with E_c = 21.8 GPa in order to account for the influence of long-term creep of concrete at the interfaces.
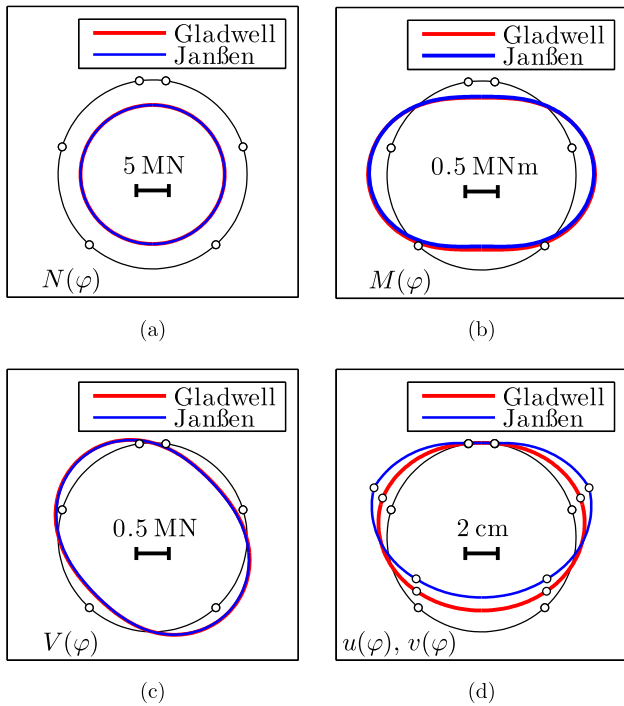

Fig. 9. Structural behavior of the analyzed segmental tunnel ring subjected to ground pressure, with K = 0.722 and σ_v = 1.217 MN/m²: (a) normal force, (b) bending moment, (c) shear force, and (d) deformed configuration; red lines refer to Gladwell's model, evaluated with E_c = 43.6 GPa, blue lines to Janßen's model, evaluated with E_c = 21.8 GPa, in order to account for the influence of long-term creep of concrete at the interfaces. (For interpretation of the references to color in this figure legend, the reader is referred to the web version of this article.)

motivation to study the temporal evolution of the ovalization of the circular cross-section of the tunnel ring in a continuous fashion. To this end, Janßen's model is extended towards consideration of the time-dependent behavior of concrete. Because the bending moments are virtually constant and in agreement with (i) the underlying assumption of a linear stress distribution in the segment-to-segment contact area, see Section 3.2, and (ii) the assumption of linear creep of concrete, the elastic compliance, $1/E_c$, is replaced in Eqs. (35 and 36) by the creep compliance function of the B4 model, $J(t, t_0)$, see Appendix B for more details:

$$\Delta\theta = \frac{12\,J(t, t_0)}{b\,h^2} \cdot M, \qquad |e| \leqslant h/6, \tag{47}$$

$$\Delta\theta = \frac{12\,J(t, t_0)}{b\,h^2\,\dfrac{27|e|}{2h}\left(1 - \dfrac{2|e|}{h}\right)^2} \cdot M, \qquad h/6 \leqslant |e| \leqslant h/2. \tag{48}$$

Eqs. (47) and (48) represent an approximate approach, because the evolution of the interfacial eccentricities results in an evolution of the size of the compressed zones and, thus, the normal stresses are not strictly constant throughout the analyzed period of time. Considering, as before, σ_v = 1.217 MN/m² and K = 0.722, the nonlinear structural problem is solved for several time instants, covering a period of 100 years. At the end of this period, the time-dependent ovalization displacements will have reached more than 60 % of the displacement at the initial time instant. Leonhardt and Reimann's recommendation of performing a time-*independent* analysis, which is based on an elastic compliance multiplied by a factor of 2, refers to a duration of ground pressure action of 1.26 years, see the white-filled circles in Fig. 10(a). Given that creep of concrete is nowadays known to increase progressively, without approaching an asymptotic limit, suggests to increase the elastic compliance rather by a factor of 3 instead of 2.

Given that creep has a significant influence on the structural displacements, but only a small influence on the distributions of the inner forces, provides the motivation to compute elastic limit values of the ground pressure for different values of K in context of time-independent structural analysis. Thereby, the behavior of the unreinforced interfaces is compared with the performance of bolted interfaces.

4.3. Elastic limit analysis: unreinforced interfaces vs. bolted interfaces

The following structural sensitivity analysis refers to the elastic limits of segmental tunnel rings with (i) unreinforced interfaces and (ii) bolted interfaces, respectively. Both cases are described, based on the nonlinear interface model of Section 3.3. The nonlinearities resulting from segment-from-segment separation are taken into account. However, the analysis is restricted to linear material behavior of concrete and steel, such that either the onset of crushing of concrete or the onset of yielding of steel defines the elastic limit.

As long as the material behavior of concrete and steel is linear-elastic, the structural behavior of a segmental tunnel ring is a *linear* function of the ground pressure. This implies that the nonlinear solution scheme described in Section 4.1 needs to be applied only once for any specific value of K. An arbitrary intensity of the ground pressure may be chosen for this task. Determination of the eccentricities at the interfaces is a nonlinear problem, which is solved iteratively as previously
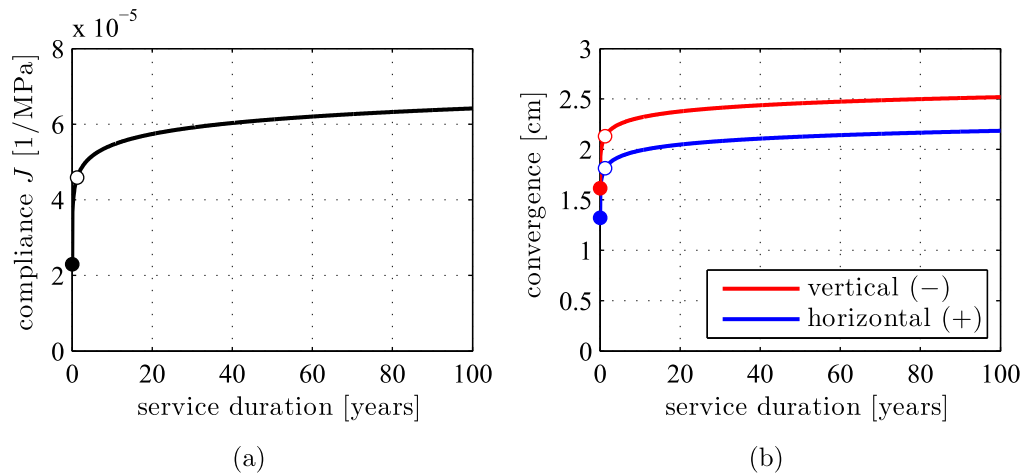
Fig. 10. Influence of creep of concrete at segment-to-segment interfaces on the structural behavior of the segmental tunnel ring of Fig. 7: temporal evolutions of (a) the effective compliance of concrete according to the B4 model, see Appendix B, and (b) the convergences under the action of ground pressure with $\sigma_v = 1.217$ MPa and $K = 0.722$; "+" and "−" refer to an increase and a decrease, respectively, of the initial diameter.
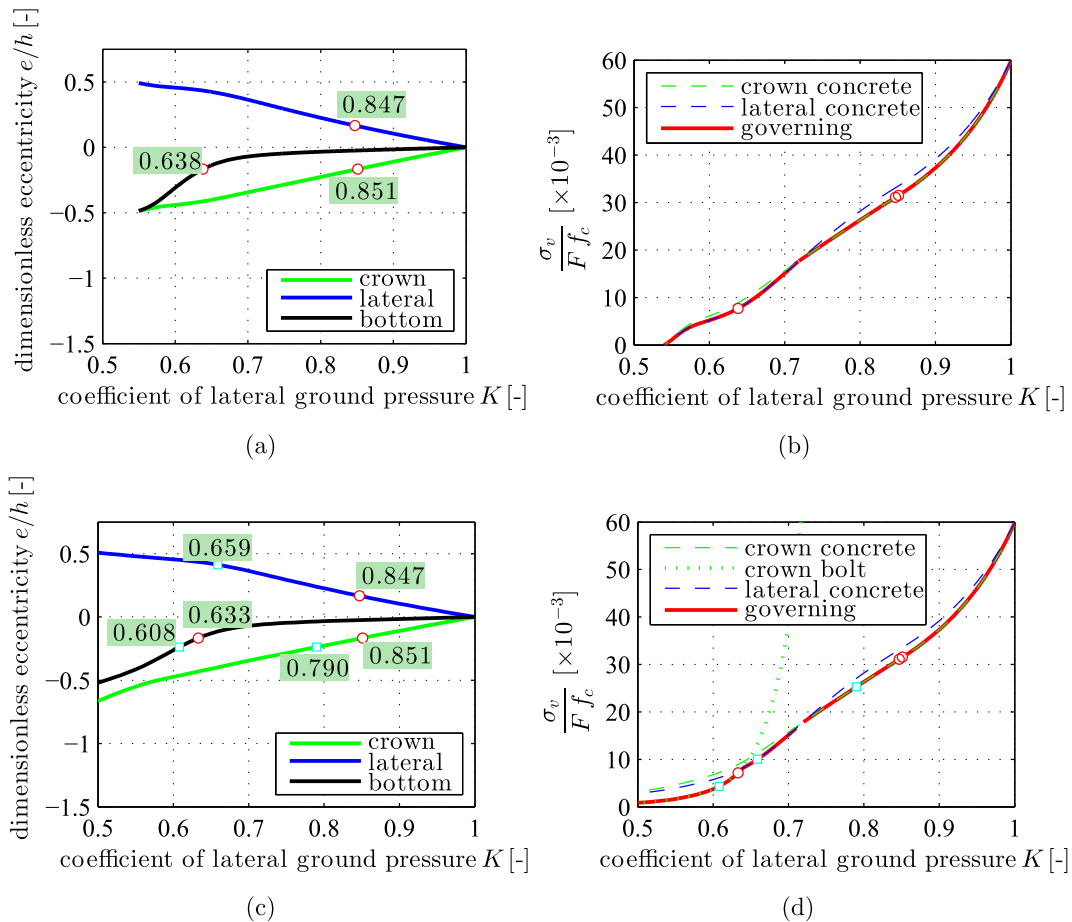

Fig. 11. Results from elastic limit analysis of the segmental tunnel ring of Fig. 7 as a function of the coefficient of lateral ground pressure; unreinforced interfaces: (a) and (b); bolted interfaces: (c) and (d); interfacial eccentricities as a function of K: (a) and (c); elastic limit intensities of the vertical ground pressure as a function of K: (b) and (d).

described. The solution obtained for the considered value of K scales *linearly* with the intensity of the ground pressure. This facilitates the calculation of elastic limits. The elastic limit intensity of the vertical ground pressure decreases with decreasing values of the coefficient of lateral ground pressure, see Fig. 11.

Results from the performed sensitivity analysis provide detailed insight into the structural performance of segmental tunnel rings with

unreinforced or bolted interfaces:

• As long as full-face contact prevails in all interfaces ($K > 0.851$), the bolts are not active. Therefore, unreinforced and bolted interfaces result in *the same* structural behavior, see Fig. 11. Thereby, the elastic limit of the segmental tunnel ring is governed by the onset of crushing of concrete at the crown interfaces.
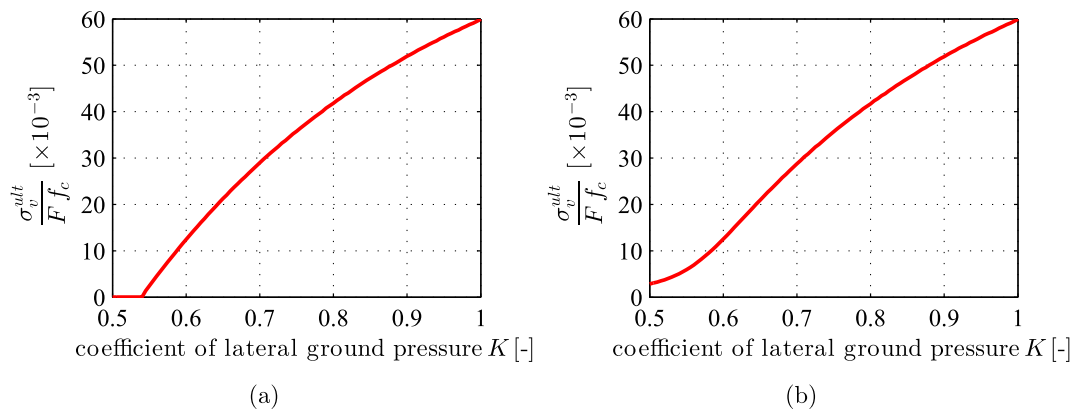
Fig. 12. Results from bearing-capacity analysis of the segmental tunnel ring of Fig. 7: bearing-capacity intensities of vertical ground pressure as a function of the coefficient of lateral ground pressure for segmental tunnel rings with (a) unreinforced interfaces, and (b) bolted interfaces.

- Separation starts at the crown interfaces at $K = 0.851$, and at the lateral interfaces at $K = 0.847$, see the corresponding red circles in Fig. 11. Reduction of K below 0.851 increases the separation of these interfaces.

- The separation fronts at the two crown interfaces reach the bolts at $K = 0.790$, see the cyan square in Fig. 11(d). Thus, tensile forces are activated in the crown bolts. If K is further reduced, the structural behavior of the tunnel ring with unreinforced interfaces is at least slightly *different* from that with bolted interfaces.

- Because of load redistributions associated with a further decrease of K, the degree of utilization at the lateral interfaces increases relative to that at the crown interfaces. At $K = 0.719$, crushing of concrete at the lateral interfaces starts to govern the elastic limits of the tunnel ring, see the intersection of the dashed blue and the dashed green curves in Fig. 11(b) and (d).

- The bolts of the lateral interfaces are activated at $K = 0.659$, see the cyan square in Fig. 11(d). Still, at that value of K, both the interfacial eccentricities and the elastic limits associated with the unreinforced interfaces and with bolted interfaces, respectively, are still very similar, compare Fig. 11(a) and (c) as well as Fig. 11(b) and (d).

- Separation in the bottom interfaces starts at $K = 0.638$, in case of unreinforced interfaces, and at $K = 0.633$, in case of bolted interfaces, see the corresponding red circles in Fig. 11. As for the tunnel ring with unreinforced interfaces, the onset of crushing of concrete in the lateral interfaces continues to govern the elastic limit of the structure, see Fig. 11(b).

- Progressive reduction of K results in an increase of the bending moments in the segmental tunnel ring. At $K = 0.638$, the onset of yielding of the bolts in the crown interfaces starts to be responsible for the elastic limits of the tunnel ring with bolted interfaces, see the intersection of the blue dashed and green dotted graphs in Fig. 11(d).

- The bolts in the bottom interfaces get active at $K = 0.608$, see the cyan square in Fig. 11(d). Around that value of K, the elastic limit of the structure with unreinforced interfaces is surprisingly *larger* than that of the structure with bolted interfaces, compare Fig. 11(b) and (d).

- The unreinforced interfaces result in a kinematic mechanism of the structure as K approaches 0.54. Thus, the elastic limit tends to zero, see Fig. 11(b). For values of K smaller than 0.54, the bolts finally become beneficial. Bolted interfaces prevent the development of a kinematic mechanism. Still, the corresponding elastic limit intensities of the vertical ground pressure are rather small, see Fig. 11(d), and the eccentricities at the crown interfaces and the lateral interfaces increase significantly with decreasing value of K, see Fig. 11(c).

Two conclusions can be drawn from the presented results. On the one

hand, the differences of the elastic limit of tunnel rings with unreinforced interfaces and bolted interfaces, respectively, are surprisingly small. This can be explained as follows: With or without bolts, the bending stiffness of the interfaces remains very small compared to that of the steel-reinforced concrete segments. On the other hand, the bolts result in a *decrease* of the elastic limit intensity of the ground pressure, for many values of K. This can be explained as follows: Segmental tunnel rings are statically indeterminate structures. Thus, stiffer parts of the structure "attract" internal forces. This explains why bolted interfaces attract slightly more internal forces than unreinforced interfaces. Furthermore, it explains why bolted interfaces may exhibit smaller elastic limits than unbolted interfaces.

In the context of the investigated elastic limits of segmental tunnel rings, the use of bolted interfaces (rather than unreinforced interfaces) was clearly beneficial in case of values of K smaller than 0.556. This provides the motivation to check whether or not the benefit of bolts is larger when approaching the bearing capacity of segmental tunnel rings.

4.4. Bearing capacity analysis: unreinforced interfaces vs. bolted interfaces

The results of the elastic limit analyses are taken as the starting point for the analysis of the bearing capacity. Thereby, nonlinear material behavior of concrete and steel is considered as explained in Section 3.3. The simulations refer to several values of K in the interval $0.5 \leqslant K \leqslant 1.0$. For each value of K, the intensity of the ground pressure is increased until plastic hinges develop at two pairs of interfaces and the structure fails by means of developing a kinematic mechanism. A plastic hinge implies that the steel of the bolt is yielding and that concrete has reached the crushing stress $F f_c'$ in the segment-to-segment contact region.

The bearing capacity of segmental tunnel rings with unreinforced interfaces and bolted interfaces decreases with decreasing coefficient of lateral ground pressure, see Fig. 12(a) and (b). The bolts do not result in a significant increase of the bearing capacity for values of K larger than 0.60. For bending-dominated scenarios of even smaller values of K, in turn, the bolts result in a significant increase of the bearing capacity of the segmental tunnel ring.

It is noteworthy that the mechanical behavior of the segments was modeled, as linear-elastic. Nonlinear material behavior was assumed to be restricted to the interface regions. Consequently, the structural simulations are based on the assumption that the nonlinear behavior of the interfaces governs the failure of segmental tunnel rings. This agrees with conclusions by Luttikholt (Luttikholt, 2007; Luttikholt et al., 2008). Still, it provides the motivation to check whether or not the chosen modeling approach delivers reliable results of the bearing capacities. This check is carried out in the context of re-analyzing a bearing-capacity test on a segmental tunnel ring.
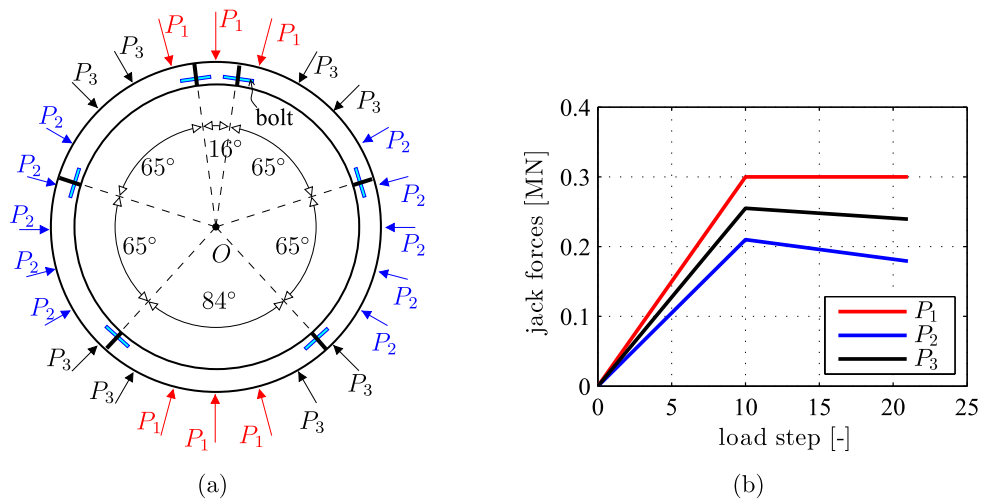
Fig. 13. Bearing-capacity test on a segmental tunnel ring (Liu et al., 2016): (a) layout of the hydraulic jacks and (b) imposed jack forces.
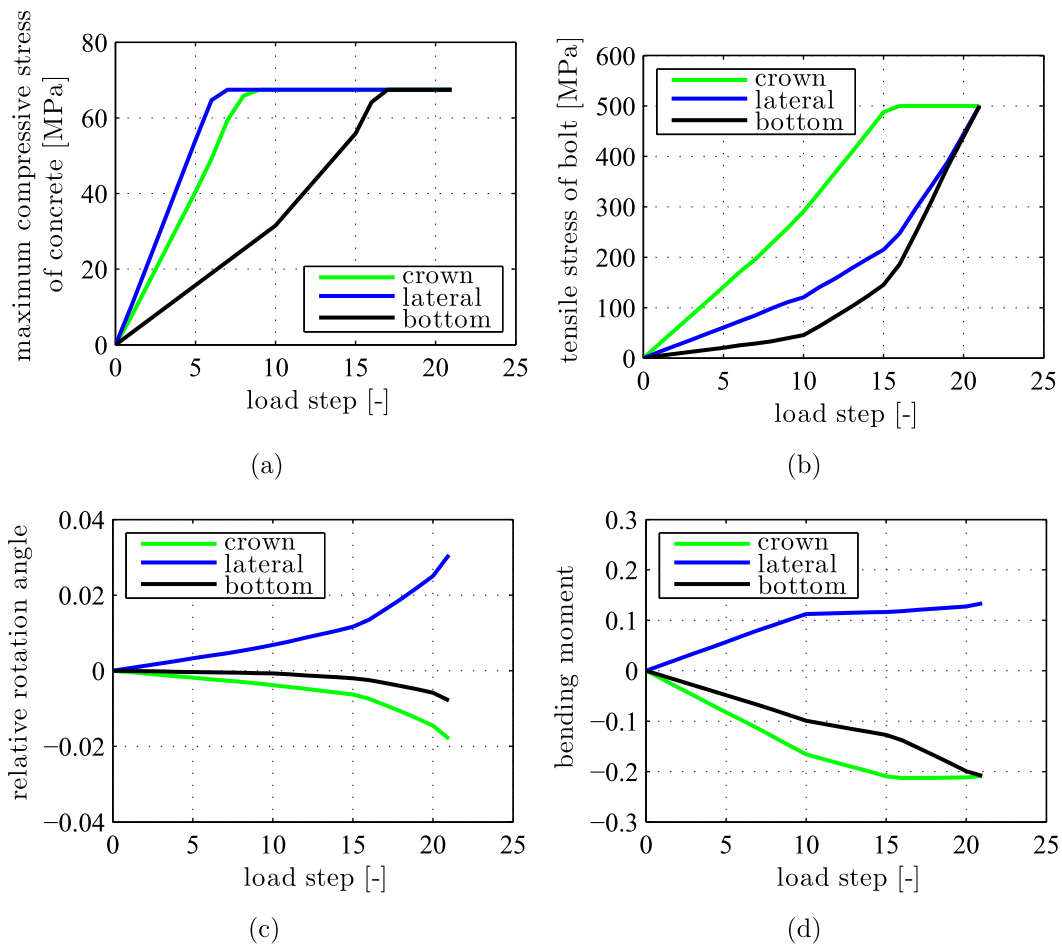

Fig. 14. Re-analysis of the bearing-capacity test of the segmental tunnel ring: evolution of (a) the maximum compressive stresses of concrete, (b) the tensile stresses of the bolts, (c) the relative rotation angles at the interfaces, and (d) the bending moments.

5. Is the overall bearing capacity of segmental tunnel rings indeed governed by the local bearing capacity of segment-to-segment interfaces?

In this section, a bearing-capacity test on a segmental tunnel ring, subjected to radial point loads, is analyzed, based on the combination of the linear transfer relations from Section 2 and the nonlinear interface model for bolted interfaces from Section 3.3.

5.1. Bearing-capacity test on a segmental tunnel ring subjected to point loads (Liu et al., 2016)

The tested ring is similar to the one analyzed in Section 4, see Fig. 7 and Table 1. Anisotropic ground pressure was simulated by 24 hydraulic jacks, exerting radial point loads onto the tunnel ring, see Fig. 13(a). The point loads were equally distributed at angular positions $\varphi_p = (p - 1) \cdot 15°$, $p = 1, 2, ..., 24$. Three different intensities of point

loads were prescribed. Point loads P_1 were acting in the top and bottom regions, point loads P_2 in lateral regions, and point loads P_3 in the intermediate regions, see Fig. 13(a).

The load-controlled test was organized as follows. In the first 10 loading steps, the point loads were increased proportionally with ratios $P_1{:}P_2{:}P_3 = 1.00{:}0.70{:}0.85$, up to the force levels $P_1 = 0.300$ MN, $P_2 = 0.210$ MN, and $P_3 = 0.255$ MN, see Fig. 13(b). Subsequently, P_1 was held constant. The lateral point loads (P_2) were decreased progressively by 0.0028 MN/step. The intermediate point loads (P_3) were set equal to the average of P_2 and P_1. During this unloading phase, the test had to be stopped at load step 21, because the displacements of the structure grew so large that the development of a kinematic mechanism was practically reached (Liu et al., 2016). At that last load step, the point load amounted to $P_1 = 0.300$ MN, $P_2 = 0.179$ MN, and $P_3 = 0.240$ MN.

5.2. Model validation by comparing the predicted and the experimentally obtained bearing capacity of the segmental tunnel ring

Structural analysis of the bearing capacity test is based on the linear transfer relations. They are evaluated for 30 sets of load integrals. 24 sets refer to the *known* point loads, see Eqs. (21)–(26). The remaining six sets refer to the *unknown* relative rotation angles of the six interfaces, $\Delta\theta_1$, $\Delta\theta_2$, …, $\Delta\theta_6$, see Eqs. (9)–(12). The symmetry of the problem at hand implies that $\Delta\theta_6 = \Delta\theta_1$, $\Delta\theta_5 = \Delta\theta_2$, and $\Delta\theta_4 = \Delta\theta_3$. Thus, the number of unknowns is reduced from six to three. The transfer relations are combined with the nonlinear interface model for bolted interfaces, see Section 3.3. The numerical calculations are carried out as described in Section 4.1.

The structural analysis provides insight into the nonlinear behavior of the segmental tunnel ring, see Fig. 14. Already during the initial loading phase, the point loads result in an amount of bending of the ring such that significant segment-from-segment separation activates all three groups of interfacial bolts, see the progressively increasing bolt stresses in Fig. 14(b). Also, crushing of concrete starts already during the initial loading phase: at the lateral interfaces at load step 7, and at the crown interfaces at load step 9, see Fig. 14(a).

During lateral unloading, the structure undergoes a stepwise degradation. At load step 16, the steel bolts of the crown interfaces start to yield, see Fig. 14(b). At load step 17, crushing of concrete starts at the bottom interfaces, see Fig. 14(a). At the final load step 21, the bolts in both lateral and bottom interfaces start yielding simultaneously, see Fig. 14(b). The rotation angles of the crown, the lateral, and the bottom interfaces increase from load step 20 to load step 21 by 24 %, 22 %, and 35 %, respectively, while the bending moments transmitted across these interfaces change only by -1 %, 5 %, and 5 %, respectively, see Fig. 14(c) and (d). At load step 21, all six interfacial bolts were yielding and the compressive stresses of concrete were almost uniformly distributed and equal to the maximum stress $F\!f_c$, see Fig. 15. This shows
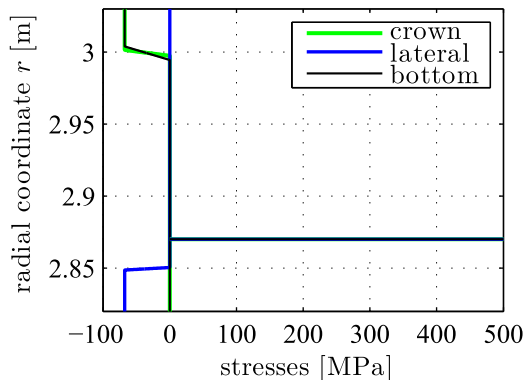

Fig. 15. Distribution of stresses at the three pairs of interfaces, computed at load step 21.

that plastic hinges were formed at almost all interfaces. In order to check whether or not it is possible to continue the structural simulation, an additional load step was considered, but no convergence was found. This agrees with the experimental observation that load step 21 was indeed very close to the bearing capacity of the tested tunnel ring. In other words, structural analysis based on *linear* transfer relations and a *nonlinear* interface model is capable of determining bearing capacities. This underlines that the overall bearing capacity of segmental tunnel rings is indeed governed by the local bearing capacity of segment-to-segment interfaces.

6. Conclusions

In the present paper, scenarios were considered where (i) relaxation of concrete has significantly reduced the excavation-related axial forces of segmental tunnel linings (Arnau et al., 2012), and (ii) creep of the ground mass has led to a ground pressure distribution very similar to the initial in-situ stress state (Lee et al., 1999). Structural analyses of segmental tunnel rings were based on the combination of linear transfer relations, representing analytical solutions of the *linear* theory of slender circular arches (Zhang et al., 2017) with *time-dependent* and *nonlinear* interface models. As for this new mode of structural analysis, the following conclusions are drawn:

- The combination of transfer relations and interface models allows for a predominately analytical mode of structural analysis. Numerical and iterative solution procedures related to nonlinearities resulting from the interfaces are limited to the possible minimum.
- The proposed mode of structural analysis is computationally efficient. Consequently, it supports structural sensitivity analyses which require the simulation of many different types of external loading.

Structural failure of a segmental tunnel ring consisting of six segments (connected by six segment-to-segment interfaces) is the consequence of development of a kinematic mechanism, in the framework of a stiffness or a strength problem, as explained in the following.

- As for unreinforced interfaces, the studied segmental tunnel ring develops inevitably a kinematic mechanism, provided that the coefficient of lateral ground pressure, K, is smaller than or equal to 0.54. In such cases, the anisotropy of the external loading is so large that the eccentricities at the interfaces reach a level that the *compressive* normal stresses transmitted across the interfaces do no longer allow the establishment of equilibrium. Thus, the failure of the segmental tunnel ring is governed by a *stiffness* problem at the interfaces.
- Considering either bolted interfaces or unreinforced interfaces in the context of values of K in the interval $0.54 < K < 1$, the development of a kinematic mechanism requires the development of plastic hinges. The latter are related to compressive crushing of the concrete and, in case of bolted interfaces, tensile yielding of the steel. Thus, the failure of the segmental tunnel ring is governed by a local *strength* problem at the interfaces.

Segmental tunnel linings must provide reliable services for many decades. In the related context of serviceability limit states (SLS), creep of concrete at segment-to-segment interfaces deserves special attention.

- Creep of concrete at the interfaces results in a significant increases of the ovalization displacements of segmental tunnel rings. This is relevant for the long-term serviceability of segmental tunnel linings, because the ovalization of the linings must stay below tolerated limits.
- Creep of concrete increases, after an initial transition period, linearly with the logarithm of time, see e.g. (Bažant et al., 2011; Zhang
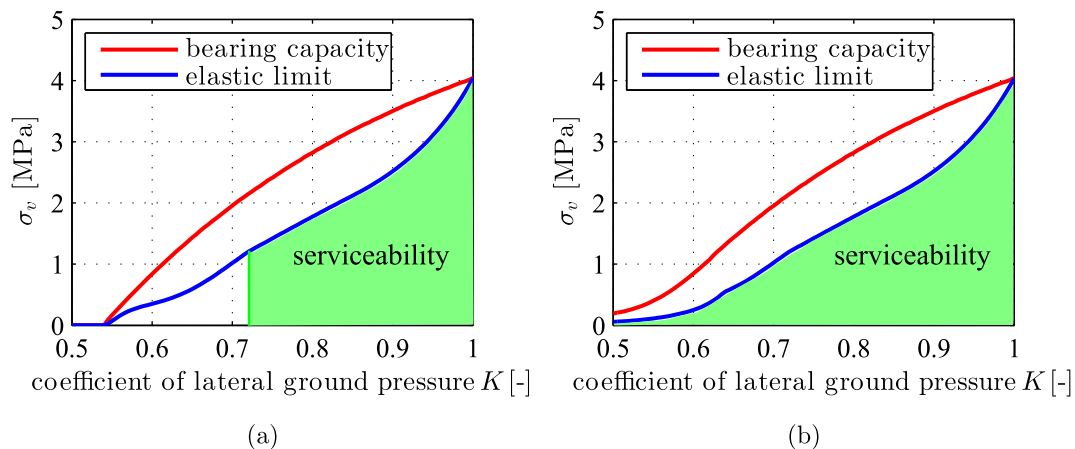
Fig. 16. Comparison of intensities of the ground pressure related to the elastic limit (blue curves) and to the bearing capacities (red curves) of the segmental tunnel ring of Fig. 7 with (a) unreinforced interfaces and (b) bolted interfaces without consideration of ring-to-ring interaction for both cases. (For interpretation of the references to color in this figure legend, the reader is referred to the web version of this article.)

et al., 2014). In other words, creep of concrete never comes to an end. Therefore, relative rotation angles at segment-to-segment interfaces increase progressively, without approaching an asymptotic limit. This calls for the future development of design rules for the SLS, based on state-of-the-art creep formulations.

- Leonhardt and Reimann recommended to account for creep of concrete hinges by performing a time-*independent* analysis. The latter is based on an "equivalent" elastic compliance of concrete, which is by a factor of 2 larger than the elastic compliance $1/E_c$. In the present paper, this approach was shown to account for a service period of 1.26 years only. Given that tunnels shall reach a service life of up to one century, the present study suggests that the "equivalent" elastic compliance of concrete should rather be 3 times larger than the elastic compliance.

As to ensure long-term durability of segmental tunnel linings, it is also desirable that segment-to-segment interfaces do not reach their elastic limits during regular service (Schlappal et al., in preparation). In this context, the following conclusions concerning the benefit of interfacial bolts are drawn:

- Bolts might appear to be counterproductive, because for many practically relevant values of K, they result in a decrease of the elastic limit intensity of the ground pressure, compare the blue curves in Fig. 16.
- Still, bolts are clearly improving the serviceability of segmental tunnel rings, when assessed from the viewpoint of the design recommendations by Leonhardt and Reimann. They recommended to limit the separation at unreinforced concrete hinges to *one half* of the initial contact area (Leonhardt and Reimann, 1965). In the present context, this implies that the eccentricities, calculated with the nonlinear interface model for unreinforced interfaces, are limited by $|e|/h \leqslant 1/3$. This separation is obtained for $K = 0.722$, independent of the actual intensity of the ground pressure, see Fig. 16(a). Even smaller values of K are associated with the risk of

segmental "snap through" (Majdi et al., 2016), at least from the viewpoint of Leonhardt and Reimann. Therefore, interfacial bolts do result in a significant increase of the serviceability of segmental tunnel rings, because they are ensuring the position stability of segmental tunnel rings, even for values of K smaller than 0.722, see Fig. 16(b).

- For a markedly anisotropic ground pressure, associated with small values of K, the use of bolts should be mandatory, because the transmission of compressive forces across unreinforced interfaces may not be sufficient in order to provide the normal force and the bending moment required for overall structural equilibrium.

As for bearing capacities associated with ultimate limit states (ULS) of segmental tunnel rings, the following conclusion is drawn:

- As for quantification of bearing capacities, it is important to carefully account for the *nonlinear* interface behavior. The mechanical behavior of the reinforced concrete segments, in turn, is of less importance. They may be modeled as *linear*-elastic. This is shown by means of re-analysis of a real-scale bearing capacity test on a segmental tunnel ring. Still, it remains desirable for future developments to extend the linear transfer relations towards consideration of damage of steel-reinforced concrete segments, such as observed during real-scale experiments using test rigs for segments (Gehwolf et al., 2017). Such an extension is the topic of a follow-up paper (Zhang et al., under revision).

Appendix A. List of symbols

A	initial contact area of the interface
A_s	cross-sectional area of the bolt
a/c	aggregate-cement ratio in the mix by weight
B	width of the cross-section of the segment
b	width of the initial contact area of the interface
C_0	compliance of concrete for basic creep
D_s	diameter of the bolt
d_c	effective length of the interface

d_s	length of the bolt
E_c	Young's modulus of concrete
E_s	Young's modulus of the bolt
EA	extensional stiffness of the segment
EI	bending stiffness of the segment
e	eccentricity of the interface
$\mathbf{e}_r$	base vector in the radial direction
e_s	eccentricity of the bolt
F	triaxial-to-uniaxial compressive strength ratio of concrete
f_c	uniaxial compressive strength of concrete
f_y	yielding stress of the bolt
H	height of the cross-section of the segment
h	height of the initial contact area of the interface
J	total compliance of concrete
K	coefficient of lateral ground pressure
M	bending moment
M_i	bending moment at the initial cross-section of the segmental tunnel ring
M_j	bending moment transmitted across the jth interface
M^L	load integral for the bending moment
N	normal force
N_i	normal force at the initial cross-section of the segmental tunnel ring
N_j	normal force transmitted across the jth interface
N^L	load integral for the normal force
N_s	number of the bolts at each interface
P	point load
P_1	point load acting in the top and bottom regions of the segmental tunnel ring
P_2	point load acting in the lateral regions of the segmental tunnel ring
P_3	point load acting in the intermediate regions between P_1 and P_2
q_r	radial component of distributed loading
q_φ	circumferential component of distributed loading
R	radius of the segmental tunnel ring
r	radial coordinate of the polar coordinate system
r_0	radial coordinate of the separation front
r_1	radial coordinate of the starting point of the plastic region of concrete
r_b	lower limit of the integral for determination of stress resultants
r_e	upper limit of the integral for determination of stress resultants
r_s	radial coordinate of the bolt
r_{cl}	radial coordinate of the closed edge of the interface
r_{op}	radial coordinate of the open edge of the interface
t	current age of concrete
t_0	age of concrete at loading time
u	radial component of displacement
u_i	radial displacement at the initial cross-section
u^L	load integral for the radial displacement
V	shear force
V_i	shear force at the initial cross-section of the segmental tunnel ring
V^L	load integral for the shear force
v	circumferential component of displacement
v_i	circumferential displacement at the initial cross-section
v^L	load integral for the circumferential displacement
w/c	water-cement ratio in the mix by weight
α_e	effective coefficient referring to the contribution of the concrete in the elastic region to the stress resultants
α_p	effective coefficient referring to the contribution of the concrete in the plastic region to the stress resultants
β_e	effective coefficient referring to the contribution of the bolt in the elastic regime to the stress resultants
β_p	effective coefficient referring to the contribution of the bolt in the plastic regime to the stress resultants
$\Delta\ell$	change of length of the effective interface region
$\Delta\ell_c$	change of length of the concrete surrounding the bolt
$\Delta\ell_s$	change of length of the bolt
$\Delta\theta$	relative rotation angle at the interface
ε_c	strain of concrete
ε_s	strain of the bolt
ν_c	Poisson's ratio of concrete
σ	stress
σ_c	stress of concrete
σ_s	stress of the bolt
σ_h	horizontal component of the ground pressure
σ_v	vertical component of the ground pressure
σ_{rr}	normal stress in the radial direction
$\sigma_{r\varphi}$	shear stress in the circumferential direction
σ_v^{ult}	intensity of the vertical ground pressure that results in the bearing capacity
θ	cross-sectional rotation angle
θ_i	rotation angle of the initial cross-section
θ^L	load integral for the cross-sectional rotation
φ	angular coordinate of the polar coordinate system
φ_j	polar position of an interface on the segmental tunnel ring
φ_p	polar position of a point load acting on the segmental tunnel ring

Appendix B. Brief overview over the B4 model (Bažant et al., 2014)

The environmental temperature for curing of segments and service of tunnel linings is assumed to be equal to 20 °C. The creep compliance function of the B4 model reads as (Bažant et al., 2014)

$$J(t, t_0) = \frac{1}{E_c} + C_0(t, t_0), \tag{B.1}$$

where t denotes current age of concrete and t_0 stands for the age of concrete when the loading is imposed. t and t_0 are measured in days. In Eq. (B.1), the first term on right side refers to the instantaneous compliance. The second term, refers to the compliance for basic creep. It reads as

$$C_0(t, t_0) = q_2 \cdot Q(t, t_0) + q_3 \cdot \ln[1 + (t - t_0)^{(0.1)}] + q_4 \cdot \ln\left(\frac{t}{t_0}\right), \tag{B.2}$$

with

$$Q(t, t_0) = Q_f(t_0)\left[1 + \left(\frac{Q_f(t_0)}{Z(t, t_0)}\right)^{r(t_0)}\right]^{-\frac{1}{r(t_0)}}, \tag{B.3}$$

$$Q_f(t_0) = [0.086(t_0)^{2/9} + 1.21(t_0)^{4/9}]^{-1}, \tag{B.4}$$

$$Z(t, t_0) = (t_0)^{-0.5}\ln[1 + (t - t_0)^{0.1}], \tag{B.5}$$

$$r(t_0) = 1.7(t_0)^{0.12} + 8. \tag{B.6}$$

In Eq. (B.2), the model parameters q_2, q_3, and q_4 are given as follows:

$$q_2 = \frac{p_2}{1\,\text{GPa}}\left(\frac{w/c}{0.38}\right)^{p_{2w}}, \tag{B.7}$$

$$q_3 = p_3 q_2 \left(\frac{a/c}{6}\right)^{p_{3a}}\left(\frac{w/c}{0.38}\right)^{p_{3w}}, \tag{B.8}$$

$$q_4 = \frac{p_4}{1\,\text{GPa}}\left(\frac{a/c}{6}\right)^{p_{4a}}\left(\frac{w/c}{0.38}\right)^{p_{4w}}, \tag{B.9}$$

where w/c and a/c denote the initial water-to-cement mass ratio and the initial aggregate-to-cement mass ratio, respectively. The numerical values of the parameters involved in Eqs. (B.1)–(B.9) are listed in Table B.1.

Table B.1
Numerical values of the parameters involved in the B4 model (Bažant et al., 2014), specified for the concrete of the interface tested by Liu et al. (2017).

$E_c = 43.6\,\text{GPa}$	$t_0 = 28\,\text{days}$	$w/c = 0.47$
$p_2 = 21.68 \times 10^{-3}$	$p_{2w} = 3.00$	$a/c = 5.57$
$p_3 = 91.57 \times 10^{-3}$	$p_{3w} = 0.40$	$p_{3a} = -1.10$
$p_4 = 2.142 \times 10^{-3}$	$p_{4w} = 2.45$	$p_{4a} = -0.90$

The numerical values of p_2, p_3, and p_4 account for the significant amount of fly-ash of the binder.

Appendix C. Closed-form expressions of the stress resultants *M* and *N*

In order to derive closed-form expressions of the stress resultants *M* and *N*, it is useful to introduce the coordinates of the separation front, r_0, the starting point of the plastic region of concrete, r_1, and the open as well as the closed edge, r_{op} and r_{cl}. r_0 and r_1 are obtained by setting Eq. (38) equal to zero and to the strain corresponding to triaxial strength of concrete, i.e. to $-Ff_c/E_c$, respectively, followed by solving the resulting relations for *r*:

$$r_0 = R - \frac{\Delta\ell}{\Delta\theta}, \tag{C.1}$$

$$r_1 = R - \frac{1}{\Delta\theta}\left(\Delta\ell + \frac{F f_c d_c}{E_c}\right). \tag{C.2}$$

r_{op} and r_{cl} depend on the sign of the prescribed relative rotation angle $\Delta\theta$:

$$r_{op} = \begin{cases} R + h/2 \ldots \Delta\theta \geqslant 0, \\ R - h/2 \ldots \Delta\theta < 0, \end{cases} \tag{C.3}$$

$$r_{cl} = \begin{cases} R - h/2 \ldots \Delta\theta \geqslant 0, \\ R + h/2 \ldots \Delta\theta < 0. \end{cases} \tag{C.4}$$

The generalized expressions of *M* and *N* read as, see Eqs. (40) and (41)

Table C.1
Numerical values of α_e, α_p, β_e, and β_p for $\Delta\theta \geqslant 0$.

No.	mathematical conditions	stress state	α_e	α_p	β_e	β_p	r_b	r_e
C1	$r_0 \geqslant r_{op}, r_1 \leqslant r_{cl}$	Full-face contact, concrete is elastic, bolt is inactive	1	0	0	0	r_{op}	r_{cl}
C2	$r_0 \geqslant r_{op}, r_{cl} < r_1 < r_{op}$	Full-face contact, concrete is partly plastic, bolt is inactive	1	1	0	0	r_{op}	r_1
C3	$r_0 \geqslant r_{op}, r_1 \geqslant r_{op}$	Full-face contact, concrete is fully plastic, bolt is inactive	0	1	0	0	r_{op}	r_{op}
C4	$r_s < r_0 < r_{op}, r_1 \leqslant r_{cl}$	Partial separation, concrete is elastic, bolt is inactive	1	0	0	0	r_0	r_{cl}
C5	$r_s < r_0 < r_{op}, r_1 > r_{cl}$	Partial separation, concrete is plastic, bolt is inactive	1	1	0	0	r_0	r_1
C6	$r_s - f_y d_s/(E_s\Delta\theta) < r_0, r_{cl} < r_0 \leqslant r_s, r_1 \leqslant r_{cl}$	Partial separation, concrete is elastic, bolt is elastic	1	0	1	0	r_0	r_{cl}
C7	$r_s - f_y d_s/(E_s\Delta\theta) < r_0, r_{cl} < r_0 \leqslant r_s, r_1 > r_{cl}$	Partial separation, concrete is plastic, bolt is elastic	1	1	1	0	r_0	r_1
C8	$r_s - f_y d_s/(E_s\Delta\theta) \geqslant r_0, r_0 > r_{cl}, r_1 \leqslant r_{cl}$	Partial separation, concrete is elastic, bolt is plastic	1	0	0	1	r_0	r_{cl}
C9	$r_s - f_y d_s/(E_s\Delta\theta) \geqslant r_0, r_0 > r_{cl}, r_1 > r_{cl}$	Partial separation, concrete is plastic, bolt is plastic	1	1	0	1	r_0	r_1
C10	$r_0 \leqslant r_{cl}$	Full-face separation	0	0	0	0	r_{cl}	r_{cl}

Table C.2
Numerical values of α_e, α_p, β_e, and β_p for $\Delta\theta < 0$.

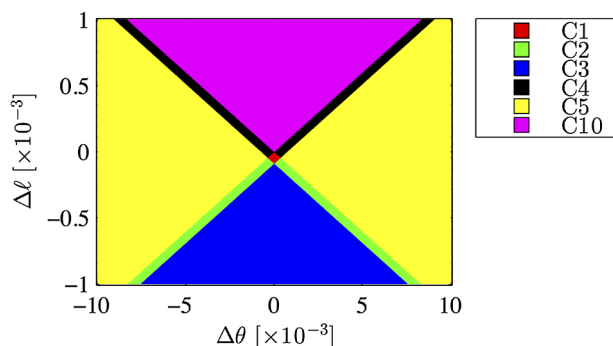| No.	mathematical conditions	stress state	α_e	α_p	β_e	β_p	r_b	r_e
C1	$r_0 \leqslant r_{op}, r_1 \geqslant r_{cl}$	Full-face contact, concrete is elastic, bolt is inactive	1	0	0	0	r_{op}	r_{cl}
C2	$r_0 \leqslant r_{op}, r_{op} < r_1 < r_{cl}$	Full-face contact, concrete is partly plastic, bolt is inactive	1	1	0	0	r_{op}	r_1
C3	$r_0 \leqslant r_{op}, r_1 \leqslant r_{op}$	Full-face contact, concrete is fully plastic, bolt is inactive	0	1	0	0	r_{op}	r_{op}
C4	$r_{op} < r_0 < r_s, r_1 \geqslant r_{cl}$	Partial separation, concrete is elastic, bolt is inactive	1	0	0	0	r_0	r_{cl}
C5	$r_{op} < r_0 < r_s, r_1 < r_{cl}$	Partial separation, concrete is plastic, bolt is inactive	1	1	0	0	r_0	r_1
C6	$r_s - f_y d_s/(E_s\Delta\theta) > r_0, r_s \leqslant r_0 < r_{cl}, r_1 \geqslant r_{cl}$	Partial separation, concrete is elastic, bolt is elastic	1	0	1	0	r_0	r_{cl}
C7	$r_s - f_y d_s/(E_s\Delta\theta) > r_0, r_s \leqslant r_0 < r_{cl}, r_1 < r_{cl}$	Partial separation, concrete is plastic, bolt is elastic	1	1	1	0	r_0	r_1
C8	$r_s - f_y d_s/(E_s\Delta\theta) \leqslant r_0, r_0 < r_{cl}, r_1 > r_{cl}$	Partial separation, concrete is elastic, bolt is plastic	1	0	0	1	r_0	r_{cl}
C9	$r_s - f_y d_s/(E_s\Delta\theta) \leqslant r_0, r_0 < r_{cl}, r_1 \leqslant r_{cl}$	Partial separation, concrete is plastic, bolt is plastic	1	1	0	1	r_0	r_1
C10	$r_0 \geqslant r_{cl}$	Full-face separation	0	0	0	0	r_{cl}	r_{cl}

Fig. C.1. Relation between the stress states C1, C2, …, C5, and C10, see details in Tables C.1 and C.2, and the prescribed values of $\Delta\theta$ and $\Delta\ell$ for an unreinforced interface.
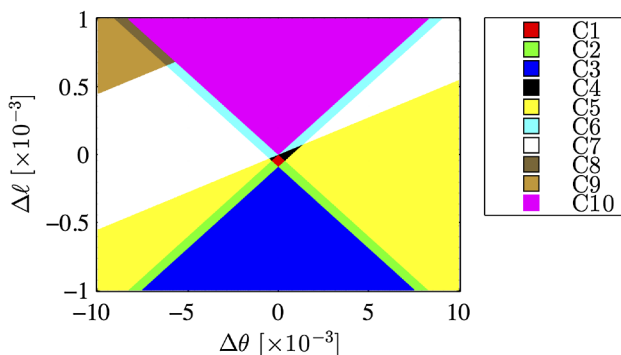

Fig. C.2. Relation between the stress states C1, C2, …, C10, see details in Tables C.1 and C.2, and the prescribed values of $\Delta\theta$ and $\Delta\ell$ for a bolted interface.

$$M = \alpha_e \cdot \frac{E_c \, b}{d_c} \left\{ \frac{\Delta \ell}{2} [(r_b - R)^2 - (r_e - R)^2] + \frac{\Delta \theta}{3} [(r_b - R)^3 - (r_e - R)^3] \right\} + \alpha_p \cdot \left[-F \, f_c \, b \, |r_{cl} - r_e| \left(\frac{r_{cl} + r_e}{2} - R \right) \right]$$

$$+ \beta_e \cdot E_s \, A_s \left[\frac{\Delta \ell}{d_s} + \frac{\Delta \theta}{d_s} (r_s - R) \right] (r_s - R) + \beta_p \cdot f_y A_s (r_s - R)$$

(C.5)

and

$$N = \alpha_e \cdot \frac{E_c \, b}{d_c} \left\{ \Delta \ell (r_e - r_b) + \frac{\Delta \theta}{2} [(r_e - R)^2 - (r_b - R)^2] \right\} + \alpha_p \cdot (-F \, f_c \, b \, |r_{cl} - r_e|)$$

$$+ \beta_e \cdot E_s \, A_s \left[\frac{\Delta \ell}{d_s} + \frac{\Delta \theta}{d_s} (r_s - R) \right] + \beta_p \cdot f_y \, A_s,$$

(C.6)

where A_s denotes the area of the bolt, α_e, α_p, β_e, β_p, r_b, and r_e are coefficients referring to the stress states at the interfaces, see Tables C.1 and C.2 as well as Figs. C.1 and C.2. In Eqs. (C.5) and (C.6), the terms starting with α_e, α_p, β_e, and β_p refer to the contribution of the concrete in the elastic region and in the plastic region and of the bolt in the elastic regime and in the plastic regime, respectively. As for unreinforced interfaces, $\beta_e = \beta_p = 0$.

References

Arnau, O., Molins, C., 2012. Three dimensional structural response of segmental tunnel linings. Eng. Struct. 44, 210–221.

Arnau, O., Molins, C., 2015. Theoretical and numerical analysis of the three-dimensional response of segmental tunnel linings subjected to localized loads. Tunn. Undergr. Space Technol. 49, 384–399.

Arnau, O., Molins, C., Blom, C., Walraven, J., 2012. Longitudinal time-dependent response of segmental tunnel linings. Tunn. Undergr. Space Technol. 28, 98–108.

Bažant, Z., Hubler, M., Yu, Q., 2011. Pervasiveness of excessive segmental bridge deflections: wake-up call for creep. ACI Struct. J. 108 (6), 766.

Bažant, Z., Hubler, M., Wendner, R., 2014. Model B4 for creep, drying shrinkage and autogenous shrinkage of normal and high-strength concretes with multi-decade applicability. TC-242-MDC multi–decade creep and shrinkage of concrete: material model and structural analysis. RILEM Mater. Struct.

Blom, C., Van der Horst, E., Jovanovic, P., 1999. Three-dimensional structural analyses of the shield-driven "Green Heart" tunnel of the high-speed line south. Tunn. Undergr. Space Technol. 14 (2), 217–224.

Caratelli, A., Meda, A., Rinaldi, Z., Giuliani-Leonardi, S., Renault, F., 2018. On the behavior of radial joints in segmental tunnel linings. Tunn. Undergr. Space Technol. 71, 180–192.

Ding, W., Yue, Z., Tham, L., Zhu, H., Lee, C., Hashimoto, T., 2004. Analysis of shield tunnel. Int. J. Numer. Anal. Meth. Geomech. 28 (1), 57–91.

Do, N.A., Dias, D., Oreste, P., Djeran-Maigre, I., 2013. 2D numerical investigation of segmental tunnel lining behavior. Tunn. Undergr. Space Technol. 37, 115–127.

Do, N.A., Dias, D., Oreste, P., Djeran-Maigre, I., 2014. Three-dimensional numerical simulation for mechanized tunnelling in soft ground: the influence of the joint pattern. Acta Geotech. 9 (4), 673–694.

El Naggar, H., Hinchberger, S.D., 2008. An analytical solution for jointed tunnel linings in elastic soil or rock. Can. Geotech. J. 45 (11), 1572–1593.

European Committee for Standardization, 2014. EN 1992-1-1:2015-07-31 Eurocode 2: Design of concrete structures – Part 1-1: General rules and rules for buildings. British Standards Institution and CEN European Committee for Standardization.

Fargnoli, V., Boldini, D., Amorosi, A., 2013. TBM tunnelling-induced settlements in coarse-grained soils: the case of the new Milan underground line 5. Tunn. Undergr. Space Technol. 38, 336–347.

Galván, A., Peña, F., Moreno-Martínez, J.Y., 2017. Effect of TBM advance in the structural response of segmental tunnel lining. Int. J. Geomech. 17 (9), 04017056.

Gehwolf, P., Wenighofer, R., Galler, R., 2017. Current status of tubbing research–insight into the research activities at the chair of subsurface engineering. Geomech. Tunnell. 10 (6), 753–759.

Gladwell, G.M., 1980. Contact Problems in the Classical Theory of Elasticity. Springer Science & Business Media.

Gong, C., Ding, W., Mosalam, K.M., Günay, S., Soga, K., 2017. Comparison of the structural behavior of reinforced concrete and steel fiber reinforced concrete tunnel segmental joints. Tunn. Undergr. Space Technol. 68, 38–57.

Han, L., Ye, G.-L., Chen, J.-J., Xia, X.-H., Wang, J.-H., 2017. Pressures on the lining of a large shield tunnel with a small overburden: a case study. Tunn. Undergr. Space Technol. 64, 1–9.

Janßen, P., 1983. Tragverhalten von Tunnelausbauten mit Gelenktübbings [Load carrying behavior of segmented tunnel linings] (Ph.D. thesis). Technische Universität Carolo-Wilhelmina zu Braunschweig, Braunschweig, (in German).

Kalliauer, J., Schlappal, T., Vill, M., Mang, H., Pichler, B., 2017. Bearing capacity of

concrete hinges subjected to eccentric compression: multiscale structural analysis of experiments. Acta Mech. 229 (2), 849–866.

Kasper, T., Meschke, G., 2004. A 3D finite element simulation model for TBM tunnelling in soft ground. Int. J. Numer. Anal. Meth. Geomech. 28 (14), 1441–1460.

Kasper, T., Meschke, G., 2006. On the influence of face pressure, grouting pressure and TBM design in soft ground tunnelling. Tunn. Undergr. Space Technol. 21 (2), 160–171.

Kavvadas, M., Litsas, D., Vazaios, I., Fortsakis, P., 2017. Development of a 3D finite element model for shield EPB tunnelling. Tunn. Undergr. Space Technol. 65, 22–34.

Lee, K., Ge, X., 2001. The equivalence of a jointed shield-driven tunnel lining to a continuous ring structure. Can. Geotech. J. 38 (3), 461–483.

Lee, K., Ji, H., Shen, C., Liu, J., Bai, T., 1999. Ground response to the construction of Shanghai Metro Tunnel-Line 2. Soils Found. 39 (3), 113–134.

Leonhardt, F., Reimann, H., 1965. Betongelenke (Concrete hinges). Deutscher Ausschuss für Stahlbeton 175, 1–33 (in German).

Li, X., Yan, Z., Wang, Z., Zhu, H., 2015. Experimental and analytical study on longitudinal joint opening of concrete segmental lining. Tunn. Undergr. Space Technol. 46, 52–63.

Liu, X., Bai, Y., Yuan, Y., Mang, H.A., 2016. Experimental investigation of the ultimate bearing capacity of continuously jointed segmental tunnel linings. Struct. Infrastruct. Eng. 12 (10), 1364–1379.

Liu, X., Dong, Z., Song, W., Bai, Y., 2018. Investigation of the structural effect induced by stagger joints in segmental tunnel linings: direct insight from mechanical behaviors of longitudinal and circumferential joints. Tunn. Undergr. Space Technol. 71, 271–291.

Liu, X., Zhang, C., Zhang, C., Yuan, Y., 2017. Ultimate load-carrying capacity of the longitudinal joints in segmental tunnel linings: illustrated with the typical segment joints of the Shanghai Metro rapid transit system. Struct. Concr. 18 (5), 693–709.

Luttikholt, A., 2007. Ultimate Limit State Analysis of a Segmented Tunnel Lining (Master's thesis). Delft University of Technology, The Netherlands.

Luttikholt, A., Vervuurt, A., den Uijl, J., 2008. Ultimate limit state analysis of a segmental tunnel lining. In: Walraven, J.C., Stoelhorst, D. (Eds.), Proceedings of the International fib Symposium 2008. Taylor & Francis Group, London, pp. 1137–1138.

Majdi, A., Ajamzadeh, H., Nadimi, S., 2016. Investigation of moment-rotation relation in different joint types and evaluation of their effects on segmental tunnel lining. Arab. J. Geosci. 9 (7), 1–15.

Marx, S., Schacht, G., 2010. Berechnungsmodelle für Betongelenke [Models for structural analysis of concrete hinges]. Prüfingenieur 36, 15–26 (in German).

Morgan, H., 1961. A contribution to the analysis of stress in a circular tunnel. Geotechnique 11 (1), 37–46.

Muir Wood, A.M., 1975. The circular tunnel in elastic ground. Geotechnique 25 (1), 115–127.

Ninić, J., Meschke, G., 2017. Simulation based evaluation of time-variant loadings acting on tunnel linings during mechanized tunnel construction. Eng. Struct. 135, 21–40.

Penzien, J., Wu, C.L., 1998. Stresses in linings of bored tunnels. Earthquake Eng. Struct. Dynam. 27 (3), 283–300.

Rubin, H., Vogel, U., 1993. Baustatik ebener Stabwerke (Frameworks for structural analysis). Stahlbau Handbuch für Studium und Praxis BAND 1 Teil A, Stahlbau-Verlagsgesellschaft mbH, Köln (in German).

Schlappal, T., Kalliauer, J., Vill, M., Gmainer, S., Mang, H., Eberhardsteiner, J., Pichler, B. Serviceability limits of concrete hinges (in preparation).

Schlappal, T., Schweigler, M., Gmainer, S., Peyerl, M., Pichler, B., 2017. Creep and cracking of concrete hinges: insight from centric and eccentric compression experiments. Mater. Struct. 50 (6), 244.

Tvede-Jensen, B., Faurschou, M., Kasper, T., 2017. A modelling approach for joint rotations of segmental concrete tunnel linings. Tunn. Undergr. Space Technol. 67, 61–67.

Wang, Z., Wang, L., Li, L., Wang, J., 2014. Failure mechanism of tunnel lining joints and bolts with uneven longitudinal ground settlement. Tunn. Undergr. Space Technol. 40, 300–308.

Winkler, B., Hofstetter, G., Lehar, H., 2004. Application of a constitutive model for concrete to the analysis of a precast segmental tunnel lining. Int. J. Numer. Anal. Meth. Geomech. 28 (7-8), 797–819.

Young, W.C., Budynas, R.G., 2002. Roark's Formulas for Stress and Strain, vol. 7 McGraw-Hill, New York.

Zhang, J.-L., Mang, H.A., Liu, X., Yuan, Y., Pichler, B. On a nonlinear hybrid method for multiscale analysis of a bearing capacity test on a real-scale segmental tunnel ring. Int. J. Numer. Anal. Methods Geomech. (under revision).

Zhang, J.-L., Vida, C., Yuan, Y., Hellmich, C., Mang, H.A., Pichler, B., 2017. A hybrid analysis method for displacement-monitored segmented circular tunnel rings. Eng. Struct. 148, 839–856.

Zhang, Q., Le Roy, R., Vandamme, M., Zuber, B., 2014. Long-term creep properties of cementitious materials: comparing microindentation testing with macroscopic uni-axial compressive testing. Cem. Concr. Res. 58, 89–98.